

# A cosmic formation site of silicon and sulphur revealed by a new type of supernova explosion

Steve Schulze<sup>1, 2\*</sup>, Avishay Gal-Yam<sup>3</sup>, Luc Dessart<sup>4</sup>, Adam A. Miller<sup>5, 1</sup>,  
 Stan E. Woosley<sup>6</sup>, Yi Yang (杨轶)<sup>7</sup>, Mattia Bulla<sup>8, 9, 10</sup>, Ofer Yaron<sup>3</sup>,  
 Jesper Sollerman<sup>11</sup>, Alexei V. Filippenko<sup>12</sup>, K-Ryan Hinds<sup>13</sup>, Daniel A. Perley<sup>13</sup>,  
 Daichi Tsuna<sup>14, 15</sup>, Ragnhild Lunnan<sup>11</sup>, Nikhil Sarin<sup>2, 16</sup>, Seán J. Brennan<sup>11</sup>,  
 Thomas G. Brink<sup>12</sup>, Rachel J. Bruch<sup>17</sup>, Ping Chen<sup>3</sup>, Kaustav K. Das<sup>18</sup>,  
 Suhail Dhawan<sup>19</sup>, Claes Fransson<sup>11</sup>, Christoffer Fremming<sup>20, 14</sup>,  
 Anjasha Gangopadhyay<sup>11</sup>, Ido Irani<sup>3</sup>, Anders Jerkstrand<sup>11</sup>, Nikola Knežević<sup>21, 22</sup>,  
 Doron Kushnir<sup>3</sup>, Keiichi Maeda<sup>23</sup>, Kate Maguire<sup>24</sup>, Eran Ofek<sup>3</sup>,  
 Conor M. B. Omand<sup>13</sup>, Yu-Jing Qin<sup>14</sup>, Yashvi Sharma<sup>14</sup>, Tawny Sit<sup>25</sup>,  
 Gokul P. Srinivasaragavan<sup>26, 27, 28</sup>, Nora L. Strothjohann<sup>3</sup>, Yuki Takei<sup>29, 15, 30</sup>,  
 Eli Waxman<sup>3</sup>, Lin Yan<sup>19</sup>, Yuhan Yao<sup>31, 12</sup>, WeiKang Zheng<sup>12</sup>,  
 Erez A. Zimmerman<sup>3</sup>, Eric C. Bellm<sup>32</sup>, Michael W. Coughlin<sup>33</sup>, Frank. J. Masci<sup>34</sup>,  
 Josiah Purdum<sup>20</sup>, Mickaël Rigault<sup>35</sup>, Avery Wold<sup>34</sup>, Shrinivas R. Kulkarni<sup>14</sup>

<sup>1</sup>Center for Interdisciplinary Exploration and Research in Astrophysics (CIERA),  
 Northwestern University, 1800 Sherman Ave, Evanston, IL 60201, USA.

<sup>2</sup>The Oskar Klein Centre, Department of Physics, Stockholm University, AlbaNova  
 University Center, Stockholm, 106 91, Sweden.

<sup>3</sup>Department of Particle Physics and Astrophysics, Weizmann Institute of Science, 234  
 Herzl St, Rehovot, 76100, Israel.

<sup>4</sup>Institut d'Astrophysique de Paris, CNRS-Sorbonne Université, 98 bis boulevard Arago,  
 Paris, 75014, France.

<sup>5</sup>Department of Physics and Astronomy, Northwestern University, 2145 Sheridan Rd,  
 Evanston, IL 60208, USA.

<sup>6</sup>Department of Astronomy and Astrophysics, University of California, Santa Cruz, CA  
 95064, USA.

<sup>7</sup>Physics Department, Tsinghua University, Beijing, 100084, People's Republic of China.

<sup>8</sup>Department of Physics and Earth Science, University of Ferrara, via Saragat 1, Ferrara,  
 44122, Italy.

<sup>9</sup>INFN, Sezione di Ferrara, via Saragat 1, Ferrara, 44122, Italy.

<sup>10</sup>INAF, Osservatorio Astronomico d'Abruzzo, via Mentore Maggini snc, Teramo, 64100,  
 Italy.

<sup>11</sup>The Oskar Klein Centre, Department of Astronomy, Stockholm University, AlbaNova  
 University Center, Stockholm, 106 91, Sweden.

<sup>12</sup>Department of Astronomy, University of California, 501 Campbell Hall, Berkeley, CA  
 94720-3411, USA.

<sup>13</sup>Astrophysics Research Institute, Liverpool John Moores University, Liverpool Science  
 Park IC2, 146 Brownlow Hill, Liverpool, L3 5RF, UK.

<sup>14</sup>Division of Physics, Mathematics and Astronomy, California Institute of Technology,  
 Pasadena, CA 91125, USA.

- <sup>15</sup>Research Center for the Early Universe, School of Science, The University of Tokyo, 7-3-1 Hongo, Bunkyo-ku, Tokyo 113-0033, Japan.
- <sup>16</sup>Nordita, Stockholm University and KTH Royal Institute of Technology, Hannes Alfvéns väg 12, 106 91, Stockholm, Sweden.
- <sup>17</sup>School of Physics and Astronomy, Tel Aviv University, Tel Aviv, 69978, Israel.
- <sup>18</sup>Cahill Center for Astrophysics, California Institute of Technology, MC 249-17, 1200 East California Blvd, Pasadena, CA 91125, USA.
- <sup>19</sup>Institute of Astronomy and Kavli Institute for Cosmology, University of Cambridge, Madingley Road, Cambridge, CB3 0HA, UK.
- <sup>20</sup>Caltech Optical Observatories, California Institute of Technology, 1200 E California Blvd, Pasadena, CA 91125, USA.
- <sup>21</sup>Astronomical Observatory, Volgina 7, 11060 Belgrade, Serbia.
- <sup>22</sup>Department of Astronomy, Faculty of Mathematics, University of Belgrade, Studentski trg 16, 11000 Belgrade, Serbia.
- <sup>23</sup>Department of Astronomy, Kyoto University, Kitashirakawa-Oiwake-cho, Sakyo-ku, Kyoto, Kyoto 606-8502, Japan.
- <sup>24</sup>School of Physics, Trinity College Dublin, The University of Dublin, Dublin, 2, Ireland.
- <sup>25</sup>Department of Astronomy, The Ohio State University, Columbus, OH 43210, USA.
- <sup>26</sup>Department of Astronomy, University of Maryland, College Park, MD 20742, USA.
- <sup>27</sup>Joint Space-Science Institute, University of Maryland, College Park, MD 20742, USA.
- <sup>28</sup>Astrophysics Science Division, NASA Goddard Space Flight Center, 8800 Greenbelt Rd, Greenbelt, MD 20771, USA.
- <sup>29</sup>Yukawa Institute for Theoretical Physics, Kyoto University, Kitashirakawa-Oiwake-cho, Sakyo-ku, Kyoto, Kyoto 606-8502, Japan.
- <sup>30</sup>Astrophysical Big Bang Laboratory, RIKEN, 2-1 Hirosawa, Wako, Saitama 351-0198, Japan.
- <sup>31</sup>Miller Institute for Basic Research in Science, 468 Donner Lab, Berkeley, CA 94720, USA.
- <sup>32</sup>DIRAC Institute, Department of Astronomy, University of Washington, 3910 15th Avenue NE, Seattle, WA 98195, USA.
- <sup>33</sup>School of Physics and Astronomy, University of Minnesota, 116 Church Street S.E., Minneapolis, MN 55455, USA.
- <sup>34</sup>IPAC, California Institute of Technology, 1200 E. California Blvd, Pasadena, CA 91125, USA.
- <sup>35</sup>IP2I Lyon / IN2P3, IMR 5822, Universite Claude Bernard Lyon 1, CNRS, Enrico Fermi, Villeurbanne, 69622, France.

\*Corresponding author(s). E-mail(s): [steve.schulze@northwestern.edu](mailto:steve.schulze@northwestern.edu);

### Abstract

The cores of stars are the cosmic furnaces where light elements are fused into heavier nuclei [1–3]. The fusion of hydrogen to helium initially powers all stars. The ashes of the fusion reactions are then predicted to serve as fuel in a series of stages, eventually transforming massive stars into a structure of concentric shells. These are composed of natal hydrogen on the outside, and consecutively heavier compositions inside, predicted to be dominated by helium, carbon/oxygen, oxygen/neon/magnesium, and oxygen/silicon/sulphur [4, 5]. Silicon and sulphur are fused into inert iron, leading to the collapse of the core and either a supernova explosion or the direct formation of a black hole [6–9]. Stripped stars, where the outer hydrogen layer has been removed and the internal He-rich layer (in Wolf-Rayet WN stars) or even the C/O layer below it (in Wolf-Rayet WC/WO stars) are exposed [10], provide evidence for this shell structure, and the cosmic element production mechanism it reflects. The types of supernova explosions that arise from stripped stars embedded in shells of circumstellar material

(most notably Type Ibn supernovae from stars with outer He layers, and Type Icn supernovae from stars with outer C/O layers) confirm this scenario [11–15]. However, direct evidence for the most interior shells, which are responsible for the production of elements heavier than oxygen, is lacking. Here, we report the discovery of the first-of-its-kind supernova arising from a star peculiarly stripped all the way to the silicon and sulphur-rich internal layer. Whereas the concentric shell structure of massive stars is not under debate, it is the first time that such a thick, massive silicon and sulphur-rich shell, expelled by the progenitor shortly before the SN explosion, has been directly revealed.

On 7 September 2021 at 09:56 (UTC dates are used throughout this paper), the public Northern Sky Survey of the Zwicky Transient Facility (ZTF) [16, 17] discovered the supernova (SN) 2021y fj at right ascension  $\alpha = 01^{\text{h}}37^{\text{m}}46^{\text{s}}.171$  and declination  $\delta = -01^{\circ}15'17''.78$  (J2000.0; *Methods Section Discovery*) [18]. A spectrum obtained with Keck/LRIS 24 hours after discovery shows a large number of narrow emission lines and P Cygni profiles from ionised silicon, sulphur, and argon (Si III–IV, S III–IV, and Ar III; *Figure 1*) superimposed on a hot blackbody spectrum ( $T \approx 15,000$  K; *Methods Section Bolometric Light Curve*), previously unobserved in any supernova [13, 19, 20]. Lines of lighter elements, which are much more common in the Universe [3] and usually detected in spectra of infant SNe [13, 21, 22], are either very weak (carbon and helium) or even completely absent (e.g., hydrogen, nitrogen). This prompted us to monitor the photometric and spectroscopic evolution at optical and ultraviolet (UV) wavelengths for the next 120 days until SN 2021y fj faded below the brightness of the host galaxy (*Supplementary Material Observations and Data Reduction*). The early spectra also reveal narrow absorption and emission lines from the interstellar medium (ISM) in the host galaxy at a redshift of  $z = 0.13865 \pm 0.00004$ , placing SN 2021y fj at a luminosity distance of  $\approx 676.4$  Mpc, assuming Planck cosmology (*Methods Section Distance*; [23]). Hereafter, all times are given with respect to the discovery time and in the rest-frame.

The Si III–IV, S III–IV, and Ar III lines are visible up to day 7.7 (i.e., up to  $\approx 5.4$  days after the time of the  $g$ -band maximum). With time, these lines become weaker, and emission lines from singly-ionised silicon and sulphur emerge (*Extended Material Figure 1*). Some lines exhibit P Cygni profiles (*Extended Material Figure 2*), which can be produced either in the SN ejecta, an expanding shell of gas expelled by the progenitor prior to the explosion, or a stellar wind. The absorption minima are at a velocity of  $1,000\text{--}1,500$  km s $^{-1}$  and the blue edge of the absorption component reaches merely  $3,000$  km s $^{-1}$ . This is significantly slower than typical SN ejecta velocities ( $\sim 10,000$  km s $^{-1}$ ; [24]), but comparable to the wind velocities of Wolf-Rayet (WR) stars [10] and similar to the velocities of expanding shells of circumstellar material (CSM) around some SNe [e.g., 11–14]. Between day 11 and 20, the blackbody spectrum subsides, and a blue pseudocontinuum dominates the emission in the optical, a tell-tale sign of interaction with CSM [25]. Superimposed are emission lines from Si II, S II, Mg I–II, He I, and O I that remain visible through our last spectrum at day 49.8 (*Extended Material Figure 1*). Considering that silicon, sulphur, and argon are the ashes of the ephemeral oxygen-burning phase that takes place less than a few years before a massive star dies [e.g., 5], it is puzzling that the early and late spectra also show helium (*Methods Section Hydrogen and Helium Content*). Helium should have been consumed during the earlier burning stages, and it is not a daughter product of the oxygen-burning phase [5].

SN 2021y fj’s unique properties vividly stand out when comparing its spectroscopic sequence to those of stripped-envelope supernovae (SESNe) that strongly interact with CSM rich in either He (Type Ibn) or C/O/Ne (Type Icn; *Figure 2, Methods Section Comparison With Interaction-powered SESNe*). Spectra of SNe Ibn and Icn obtained shortly after explosion exhibit narrow emission lines from carbon, nitrogen, oxygen, helium, or hydrogen, but no silicon and no sulphur. These differences remain well visible in the spectra obtained around maximum light. The Type Icn SNe 2019hgp and 2021csp also show P Cygni profiles with velocities similar to those of SN 2021y fj, which were interpreted as originating from a fast stellar wind [13, 14]. At late times, all objects are characterised by a blue pseudocontinuum with superimposed emission lines. Yet again, SN 2021y fj displays striking differences: conspicuous silicon and sulphur emission lines but no Ca near-infrared (NIR) triplet at  $\sim 8,500$  Å in emission (*Figure 2*), whereas the other objects show He I (SNe Ibn) and a conspicuous Ca NIR triplet in emission. Therefore, the discovery of silicon and sulphur in SN 2021y fj is not due to differences in the data quality, the timing of the observations, or the blackbody temperature. Instead, the presence of silicon and sulphur reflects true differences in the elemental composition of the CSM and, therefore, the SN progenitor. This lets us conclude that SN 2021y fj is embedded in a thick, extended CSM rich in silicon and sulphur, never observed

in any supernova before. Since SN classes are defined by the absence or presence of particular chemical elements in their spectra [26, 27], SN 2021yfj is the first member of a previously unknown SN class: Type Ien (*Methods Section A New Type of Supernova*; [28]).

SN 2021yfj is  $> 2$  mag more luminous than a typical SESN ( $M_g = -19.0$  mag for SN 2021yfj compared to  $M_g = -17.3$  mag for a typical SESN), and it has a shorter rise time from 50% peak flux (2.3 days vs. 8 days). The combination of being more luminous with a shorter rise time is inconsistent with Ni-powered SNe. The modelling of the light curve corroborates this. Solely powering by radioactive  $^{56}\text{Ni}$  or a central engine, such as a spindown of a rapidly spinning, highly magnetised neutron star, can be excluded (*Methods Section Light-Curve Modelling*). Owing to the assumptions of the two models, they do not simultaneously capture the rise, peak luminosity, and decline. The bolometric light curve (*Figure 3*), constructed from the multiband data is akin to those of interaction-powered SNe Ibn and Icn. At peak, SN 2021yfj reached  $\gtrsim 3 \times 10^{43}$  erg s $^{-1}$ , and integrating over the entire light curve yields a radiated energy of  $0.6\text{--}1 \times 10^{50}$  erg. Both values are strict lower limits because the true bolometric peak likely occurred before our multiwavelength campaign started (*Methods Section Bolometric Light Curve*). Fitting the bolometric light curve with the model of ejecta-CSM interaction from Ref. [29, 30] reproduces the photometric evolution of SN 2021yfj (*Methods Section Light-Curve Modelling*). The fit points to an ejecta mass of  $\sim 5 M_\odot$ , a CSM mass of  $> 1 M_\odot$  and  $< M_{\text{ejecta}}$ , and an explosion energy of  $(1.5\text{--}2) \times 10^{51}$  erg (*Extended Material Figure 5*). The slight tension between the model and the observations during the rise could be mitigated by more complex CSM geometries and density profiles than the ones used here.

The ubiquity of silicon and sulphur lines in the blue part of the optical spectra at early times raises the question of the silicon and sulphur abundance in the spectrum formation region. Would a low abundance be sufficient, as can happen with iron-group elements? (For example, solar-metallicity iron can easily explain the strong blanketing observed in SNe II at the recombination epoch; see, e.g., observations [31] and models [32–34].) Or, would a high abundance be necessary, as can happen for helium in SNe Ib [e.g., 35]? To address these questions, we perform exploratory radiative-transfer simulations using mock ejecta with an elemental composition similar to the O/Si shell in massive helium stars, which is the outermost shell containing a significant amount of freshly nucleosynthesised silicon and sulphur. Our model consists of an ejecta with  $3.24 M_\odot$ , a steep density profile with a power-law exponent of  $-10$  (a wind profile is excluded because of the weakness of emission lines), and a base velocity of  $1000 \text{ km s}^{-1}$ , yielding a total kinetic energy of a few  $10^{49}$  erg at that time. Furthermore, we deposit a power of  $3 \times 10^{43}$  erg s $^{-1}$  at a velocity of  $1000 \text{ km s}^{-1}$  (*Methods Section Spectral Modelling*). This simple model (shown in red in *Figure 4*) can explain the observed features (shown in black in the same figure) at  $< 4,800 \text{ \AA}$  in the discovery spectrum in terms of the relative and absolute strength as well as the line width. Increasing the mass fraction from a few percent to 30–50% yields slightly stronger features from silicon and sulphur but in growing tension with the observations (*Methods Section Spectral Modelling*). Likewise, decreasing the mass fraction below 1% gives weaker features and is, therefore, inconsistent with the observations. Based on these simulations, we conclude that a mass fraction of a few  $\times 0.01$  suffice to explain the observed features. Furthermore, to have an optically thick CSM out to  $10^{15}$  cm requires a large CSM mass of  $\sim 3 M_\odot$ . This strongly suggests that SN 2021yfj is the product of a massive star that was stripped all the way to the silicon- and sulphur-rich internal layer prior to explosion. The presence of helium cannot be explained by this model. In fact, no O- or Si-rich material in massive-star models is rich in He.

In the framework of wind-driven mass loss, the stripping of a star all the way to the O/Si shell is very challenging to explain. Pulsational pair instabilities might accomplish that [9, 36–38]. This phenomenon is predicted to occur in stars with an initial mass of 70–140  $M_\odot$ , which experience a recurrent instability from producing  $e^-e^+$  pairs during the oxygen-burning phase. The interaction between CSM shells can produce luminous transients [9, 39, 40] with properties qualitatively matching those of SN 2021yfj. In this scenario, SN 2021yfj could be the product of collisions between the last shells ejected before the star collapses into a black hole. While this model has appeal, the detection of helium cannot be readily explained and may require, for example, a binary helium star companion. The presence of helium is also an issue for the other massive-star scenarios discussed in the *Methods Section Progenitor Scenarios*, which are motivated by the star-forming host of SN 2021yfj (*Methods Section Host Galaxy*). A review of literature models involving accretion and burning of helium on the surface of a compact object does not reveal a suitable Si/S-forming scenario (*Methods Section Progenitor Scenarios*). All these models merit additional theoretical studies.

Stellar evolution theory predicts that stars nearing the end of their lives should consist of concentric shells, with hydrogen in the outermost shell and iron at the core [1–5]. However, direct observations of this shell structure are rare. WR stars experience significant mass loss toward the end of their lives, which can expose their He (WN stars) and C/O (WC/WO stars) shells [10]. Interaction-powered SNe provide an independent view of the shell structure of stars. The CSM they interact with encodes information on the surface composition of the dying star just before it explodes, free from contamination by explosion products [41–43]. Type IIn, Ibn, and Icn supernovae probe the H, He, and C/O shells, respectively. These SNe not only complement observations of Wolf-Rayet stars but also reveal how dying stars can lose part of their outer layers just before the terminal explosion. The discovery of SN 2021yfj has three important implications for stellar evolution theory: (i) it reveals a formation site of argon, silicon, and sulphur; (ii) it likely directly confirms the complete sequence of concentric shells in massive stars; and (iii) it requires the operation of processes that can strip stars down to their inner shells.

The lack of known SNe that show any similarity to the early- or late-time spectra of SN 2021yfj suggests that Type Ien SNe are intrinsically rare. The ZTF Bright Transient Survey [BTS; 44, 45], which aims to spectroscopically classify all ZTF transients that peak brighter than  $m = 18.5$  mag and is nearly 100% complete, has not identified a single SN 2021yfj-like event during its six years of operation. Thus, from the BTS, we conclude that the rate of SN 2021yfj-like events is  $< 30 \text{ Gpc}^{-3} \text{ yr}^{-1}$  [95% confidence],  $< 1/1,000$  the rate of SNeIb/c [*Methods Section Event Rate*; 46]. As future facilities, such as the Vera C. Rubin Observatory, continue to expand the discovery space for the transient Universe, there is a great deal of hope that these surveys will uncover new classes of explosive events. SN 2021yfj represents one of these rare new transients, but it is important to note that it does not significantly stand out from the population of extragalactic transients based on its photometric evolution alone (*Extended Material Figure 4*). Instead, it is the spectra that uniquely identify SN 2021yfj as belonging to an entirely new SN class: narrow silicon and sulphur lines at early times and a blue pseudocontinuum with silicon and sulphur lines at late times. This highlights the importance of spectroscopic observations and lays plain evidence that even sophisticated artificial-intelligence-powered anomaly-detection algorithms running on light curves from the Rubin Legacy Survey of Space and Time [LSST; 47] will not be able to recover every new type of transient in the LSST data stream. To detect additional SN 2021yfj-like events or discover the predicted but yet not discovered Type Id/Idn/Ie SNe (*Extended Material A New Type of Supernova*), efforts are needed that tightly couple high-throughput, medium-resolution spectrographs with long-duration, high-cadence time-domain surveys, which will naturally be provided by existing and future medium-deep surveys [16, 48–53] and the deep Rubin Legacy Survey of Space and Time [47]. The discovery of any additional SN 2021yfj-like objects will have a profound impact on our understanding of their nature.

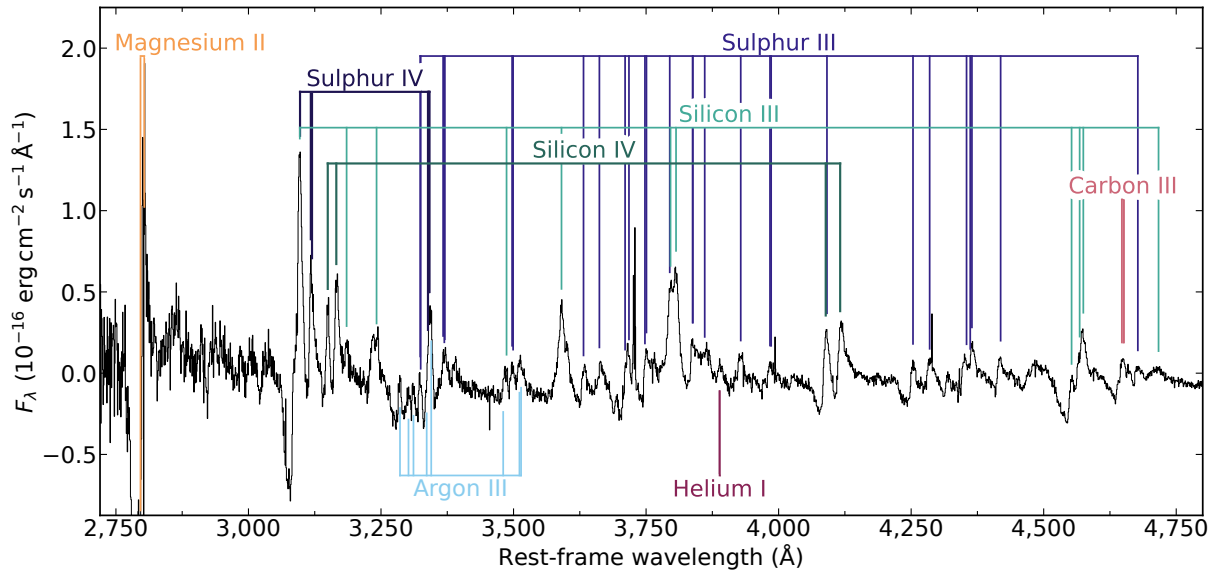


**Fig. 1:** Spectrum obtained 1.0 days after the first ZTF detection with Keck/LRIS in the range from 2,720 to 4,800 Å, after subtracting the blackbody continuum. The spectrum reveals narrow emission lines of highly ionised species of silicon, sulphur, and argon, which have never been seen in any SN before, as well as doubly ionised carbon, singly ionised magnesium, and neutral helium. A number of the highly ionised silicon and sulphur lines also exhibit P Cygni profiles with a maximum velocity of  $\sim 3,000 \text{ km s}^{-1}$  (*Extended Material Figure 2*), indicating that these lines are produced in a fast-moving, metal-rich CSM (e.g., a wind or a shell expelled by the progenitor shortly before the explosion). The spectrum is rebinned for illustration purposes. The lower bound of the ordinate axis was cropped for illustration purposes.

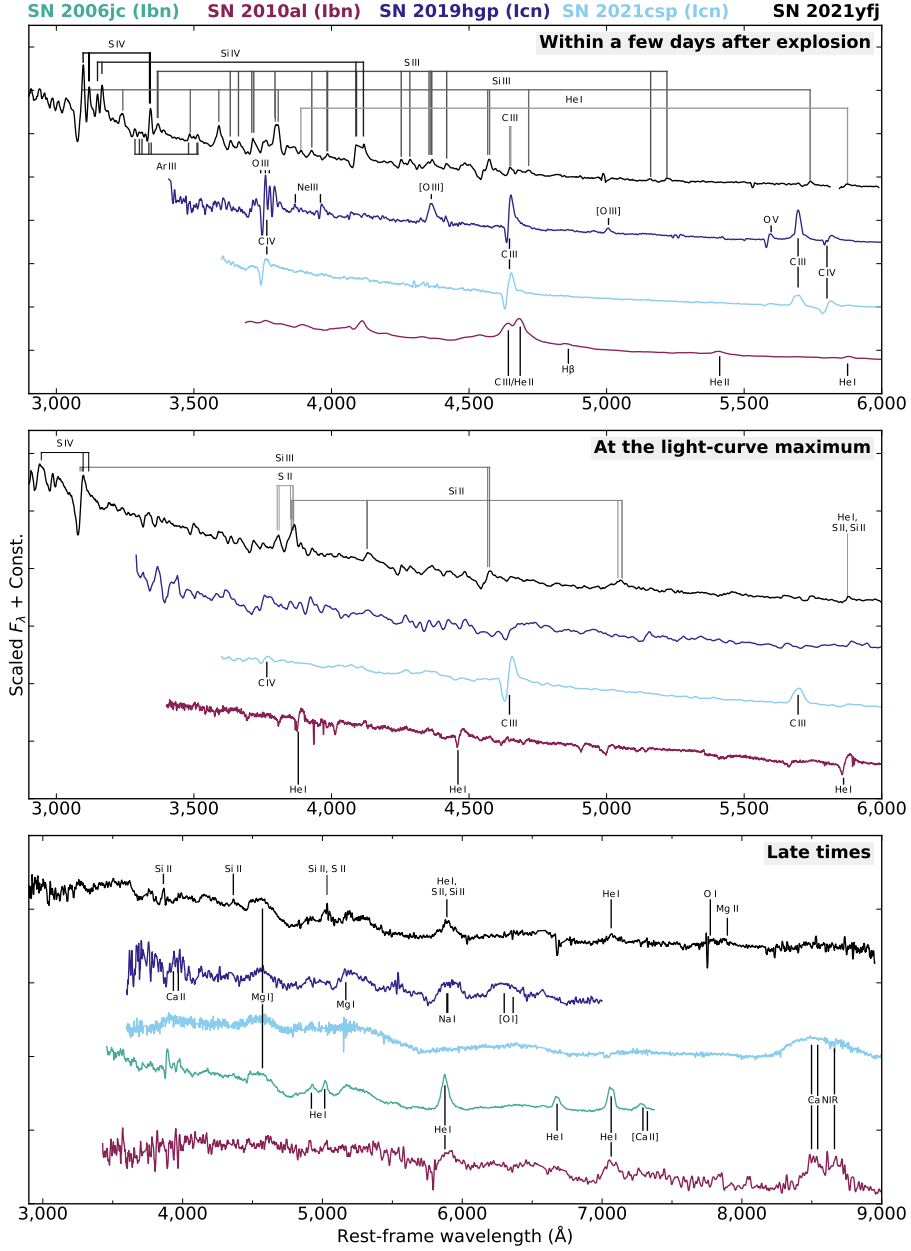


**Fig. 2: Comparison of SN 2021yfj with other interaction-powered SESNe a few days after the explosion (top), the time of maximum light (middle), and late times (bottom).** The earliest spectra of Type Ibn and Icn SNe are characterised by a hot blackbody continuum with a temperature similar to that of SN 2021yfj (*Extended Material Figure 6*). They also show lines of helium, carbon and possibly hydrogen (in SN 2010al) (Ibn), or carbon, oxygen, and neon (Icn), but no silicon, sulphur, and argon. These strong helium, carbon, oxygen, and neon lines are clearly absent in SN 2021yfj. Well after peak brightness, the spectra of SNe Ibn, Icn, and SN 2021yfj are characterised by a blue pseudocontinuum with superimposed intermediate-width (a few  $1,000 \text{ km s}^{-1}$ ) emission lines, due to the interaction of the SN ejecta and CSM. Again, SN 2021yfj shows prominent silicon and sulphur emission lines that are absent in the other objects, and the comparison objects exhibit features that are clearly absent in SN 2021yfj. Therefore, the differences between SN 2021yfj and previously known classes of interaction-powered SESNe reflect true differences in the CSM composition and the progenitor populations, making SN 2021yfj the first member of a previously unknown supernova class. All spectra are rebinned for illustration purposes.

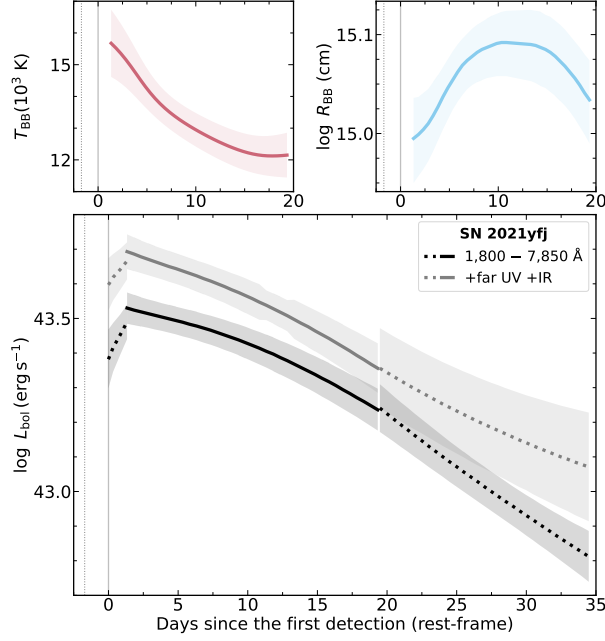


**Fig. 3:** The bolometric light curve of SN 2021y fj (bottom panel) and the evolution of the blackbody temperature (top right) and radius (top left). The bolometric light curve shown in black covers the wavelength interval from 1,800 to 7,850 Å. Correcting the bolometric flux for the missing far-UV and IR flux increases the luminosity by  $\sim 0.2$  dex. At peak brightness, SN 2021y fj reached a luminosity of  $> 3 \times 10^{43}$  erg s $^{-1}$ . Integrating over the entire light curve yields a radiated energy of  $(0.6\text{--}1) \times 10^{50}$  erg. The smaller value covers the range from 1,800 to 7,850 Å, and the larger value includes an estimate of the contribution from the far-UV and IR. Dotted lines indicate time intervals with incomplete wavelength coverage. The blackbody temperature and radius have typical values for infant interaction-powered SNe, although the gradual evolution of both properties is atypical for infant supernovae and indicative of an optically thick CSM (*Methods Section Bolometric Light Curve*). The shaded bands indicate the statistical uncertainties at the  $1\sigma$  confidence level. The vertical dotted line in each panel indicates the date of the last non-detection.



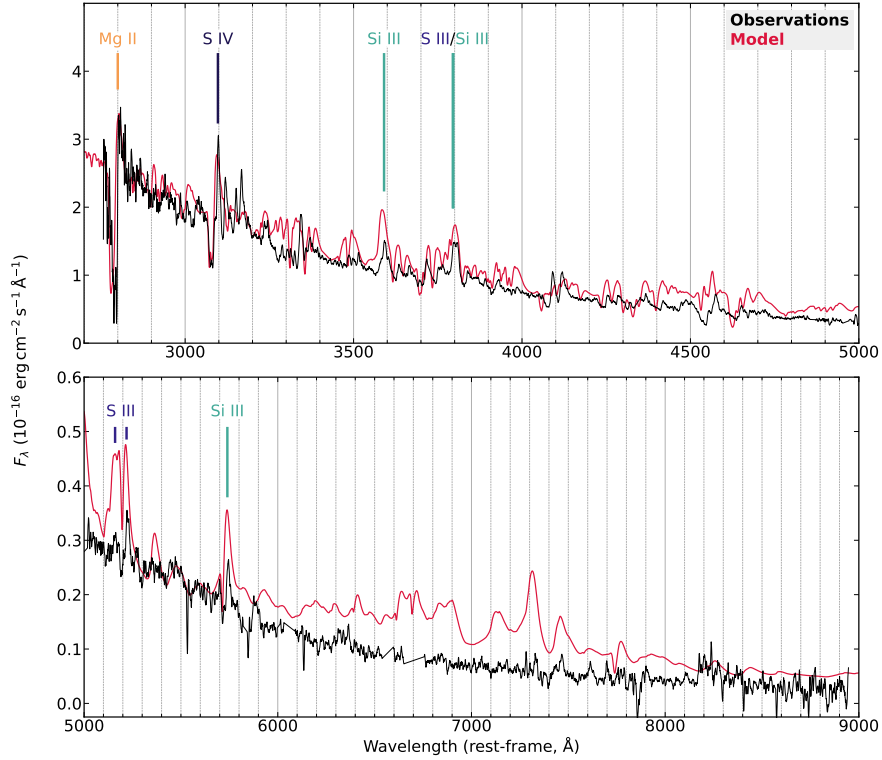
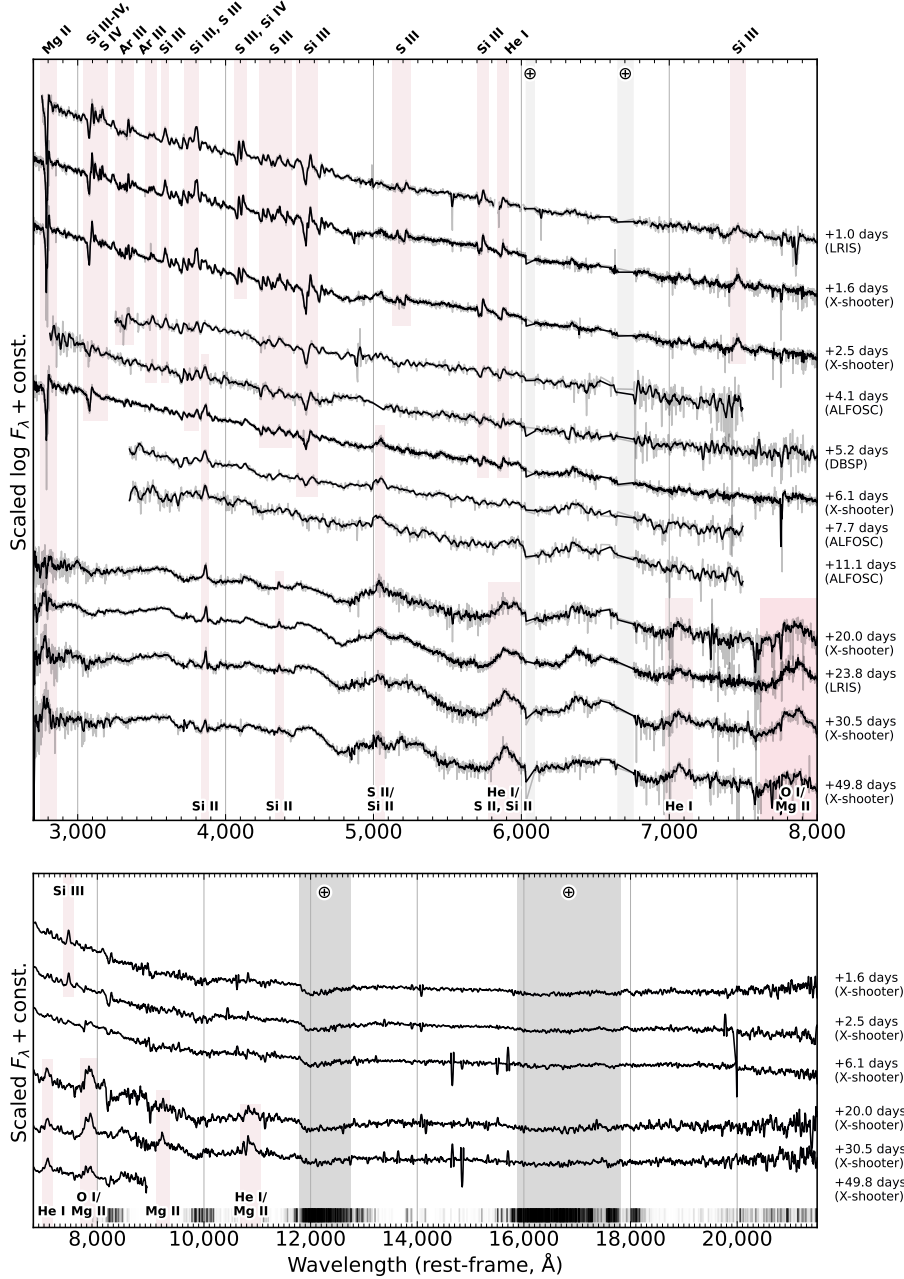


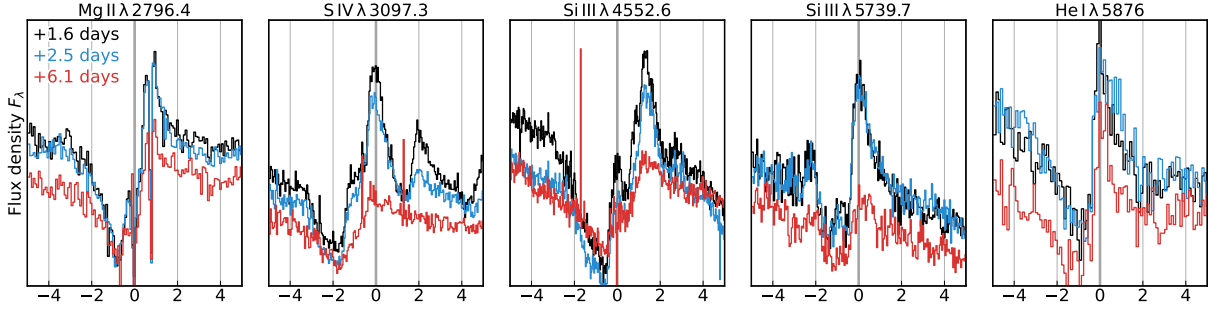
**Fig. 4: Comparison of the discovery spectrum of SN 2021yfj (black; *Figure 1*) with a spectral model (red).** The model assumes a power of  $3 \times 10^{43} \text{ erg s}^{-1}$ , an ejecta mass of  $3.24 M_{\odot}$ , a velocity of  $1000 \text{ km s}^{-1}$ , and an elemental composition similar to the O/Si shell in massive helium stars: 0.786 (oxygen), 0.1 (neon), 0.05 (silicon), 0.03 (sulphur), 0.01 (argon), 0.01 (magnesium), 0.001 (calcium), and solar abundance for iron, cobalt and nickel. The spectrum is computed with steady-state, non-local thermodynamic equilibrium radiative transfer models (for more details see the *Methods Sections Spectral Modelling*). This model matches the strongest silicon and sulphur lines and also magnesium in terms of absolute and relative strength and line width, corroborating that SN 2021yfj is likely the explosion of a massive star stripped down to its O/Si shell.

## Extended material

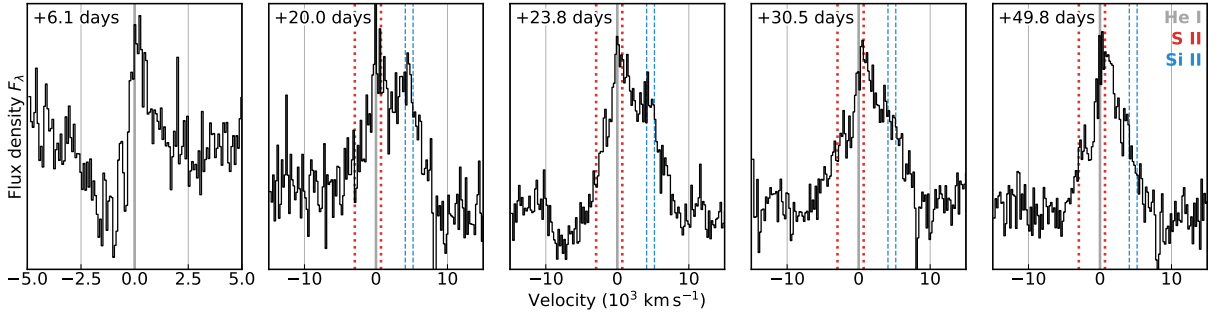


**Extended Material Fig. 1: Spectral evolution from day 1 to 49.8 of SN 2021yfj in the UV-optical (upper panel) and near IR (lower panel).** Up to day 11 the spectra are characterised by a blackbody shape with superimposed narrow emission and P Cygni lines from silicon, sulphur, argon, carbon, and helium. As the photosphere cools, the ionisation state of silicon, sulphur, and argon decreases. By day 20, a blue pseudocontinuum dominates the spectrum with superimposed intermediate-width emission lines from magnesium, silicon, sulphur, and helium. The most prominent features of both phases are marked. Regions of high atmospheric absorption are marked, and a near-IR spectrum of the opacity of Earth's atmosphere is shown as black vertical lines (black = high opacity). Host-galaxy emission lines are clipped. The original spectra are in grey, and rebinned versions are in black.

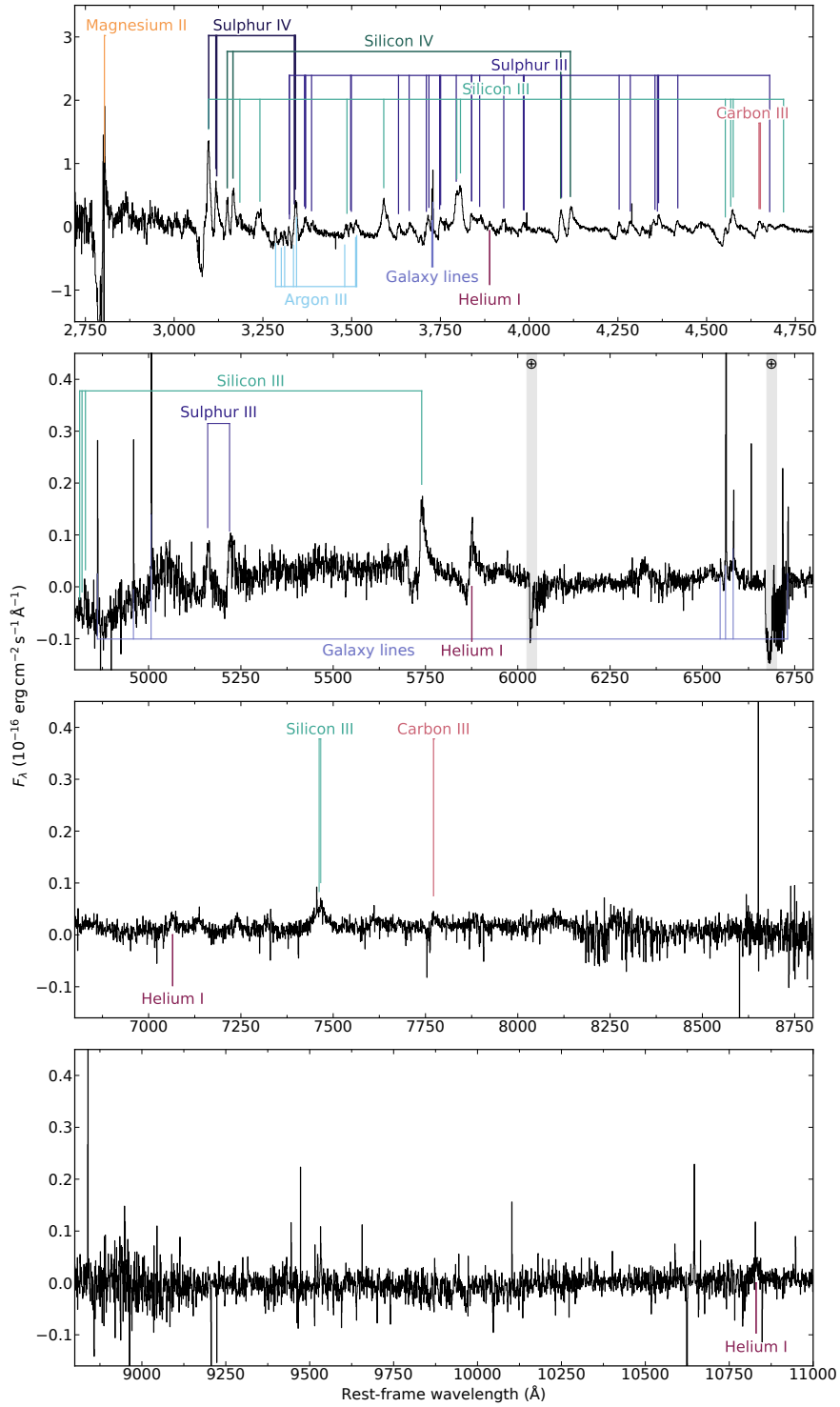
### Evolution of selected S, Si, He and Mg line profiles at early times



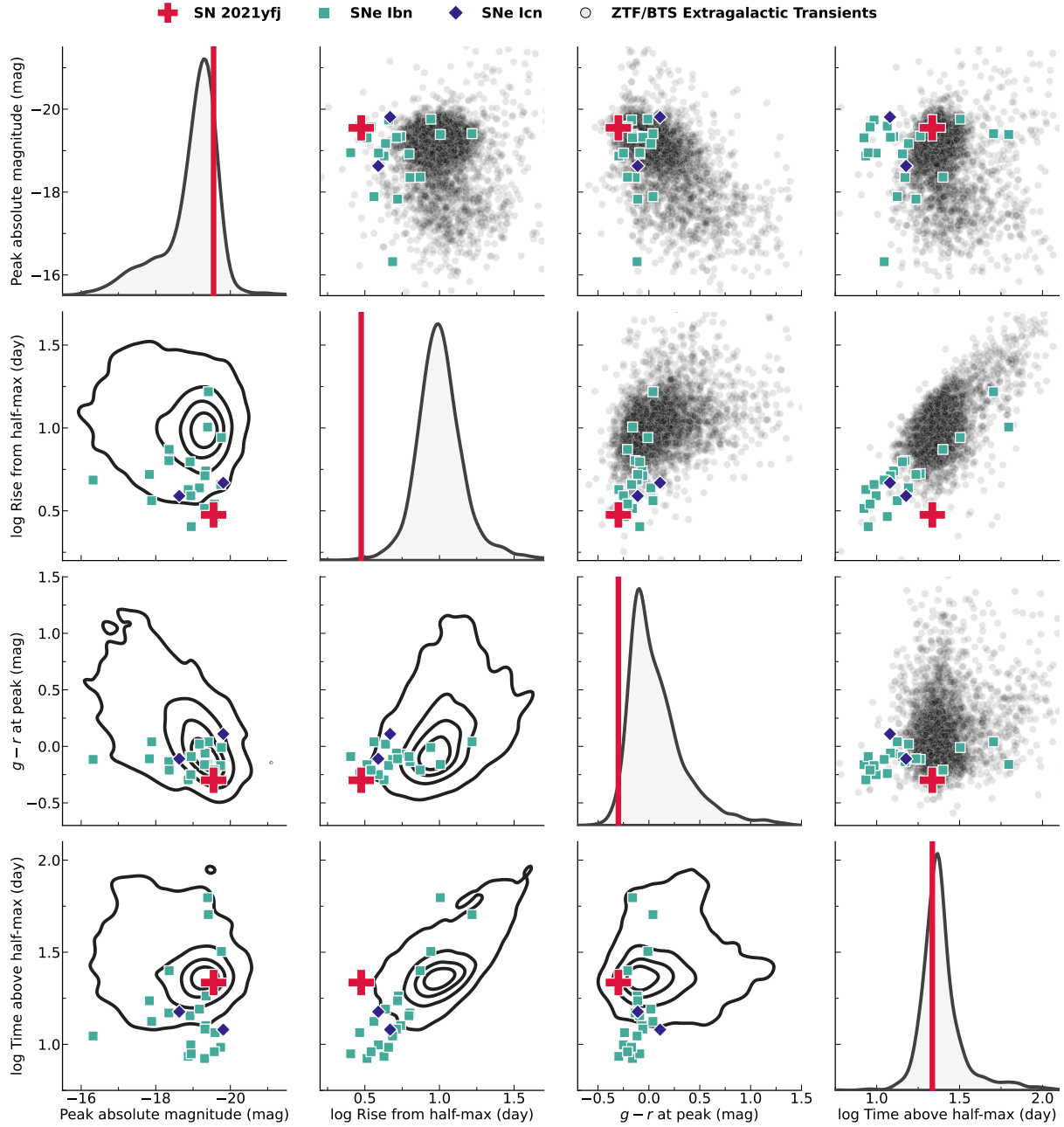
### Evolution of the 5,876 Å line



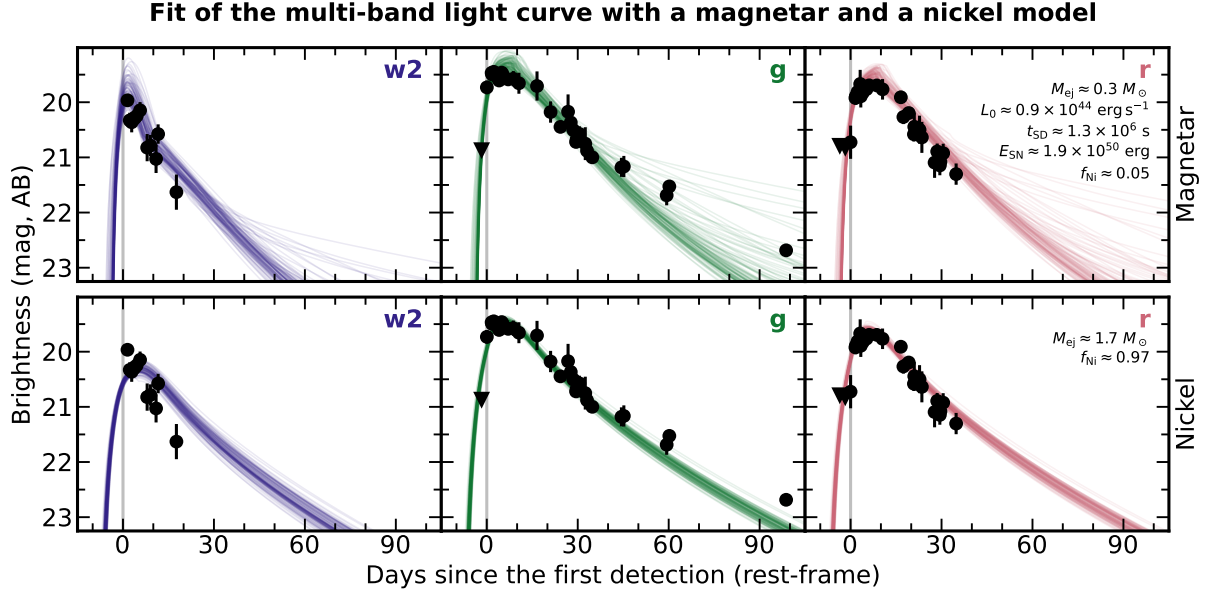
**Extended Material Fig. 2: The evolution of the line profiles of selected lines from helium, magnesium, silicon, and sulphur. *Top:*** At early times, all lines show well-developed P Cygni profiles. The absorption minima are at  $\sim 1,500 \text{ km s}^{-1}$ . The blue edge, a proxy of the maximum velocity, extends to  $\sim 3,000 \text{ km s}^{-1}$ . These velocities are comparable to velocities of stellar winds as seen in Wolf-Rayet stars [10] and winds around some SNe Icn [13, 14], and much slower than SN-ejecta velocities at similar phases ( $\sim 10,000 \text{ km s}^{-1}$ ; [54]). The Si III and Si IV lines are blended with other lines and exhibit complex line profiles. The Mg II line shows narrow absorption lines from the ISM in the host galaxy. ***Bottom:*** Up to day 6, the 5,876 Å feature shows a well-developed P Cygni profile and is dominated by He I. At later phases, this feature transitions into a pure emission line with time-variable contributions from silicon, sulphur, and helium. The spectra are rebinned for illustration purposes.



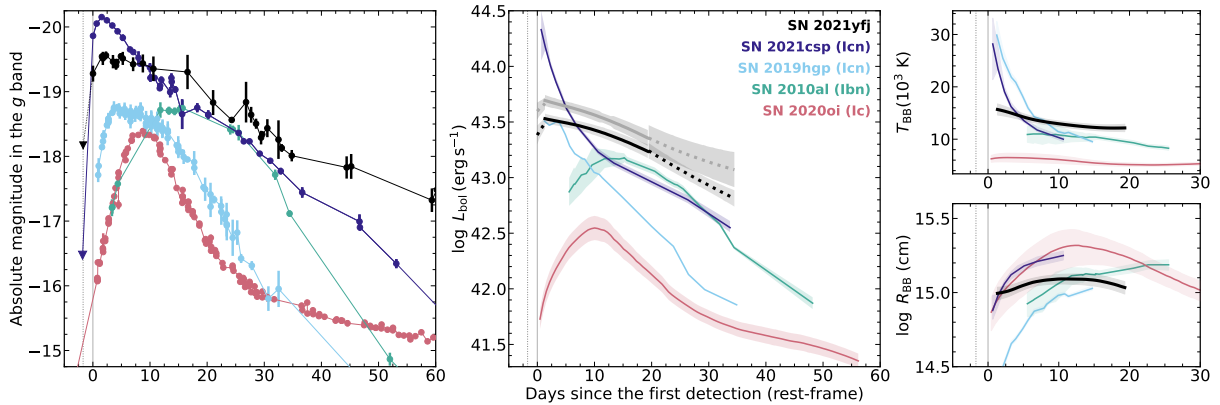
**Extended Material Fig. 3: Spectrum obtained 1.6 days after the first ZTF detection with VLT/X-shooter, after subtracting the blackbody continuum.** The full spectrum covers the wavelength range from 2,635 to 21,960 Å. The displayed wavelength range is limited to 2,720–11,000 Å where SN features are well visible. The top panel shows the same wavelength interval as the discovery spectrum in *Figure 1* obtained 12 hours earlier. The evolution between both epochs is gradual at most. In addition to the SN features, the spectrum shows emission lines from star-forming regions in the host galaxy and narrow absorption lines from the host ISM. Strong telluric features are marked with “⊕”.



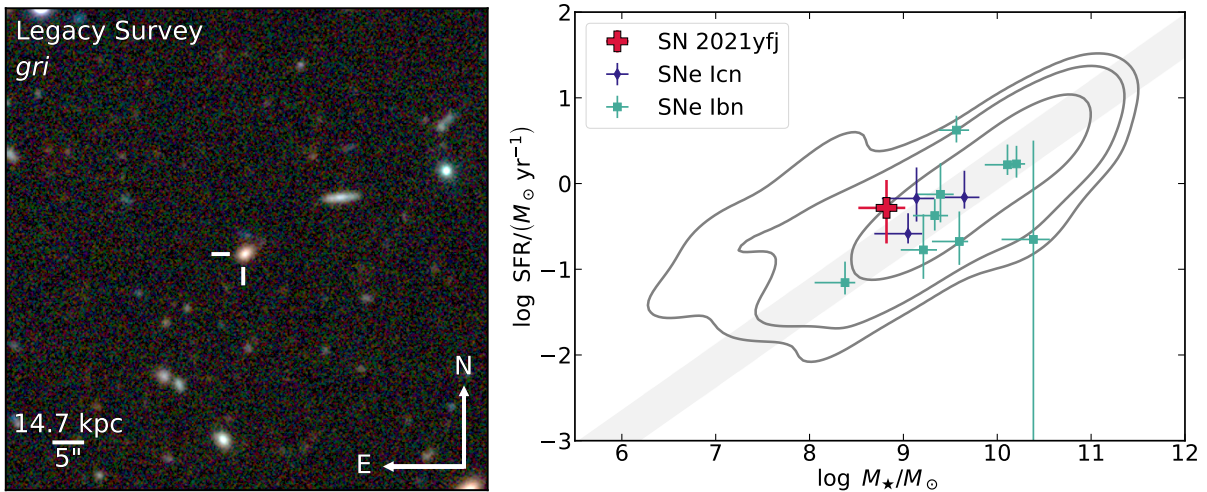
**Extended Material Fig. 4: SN 2021yfj in a 4-dimensional light-curve feature space, together with 4032 extragalactic transients from the ZTF Bright Transient Survey (79% Type Ia SNe, 11% Type II SNe, and 10% other types of core-collapse SNe and other types of transients).** The panels above the diagonal show all measurements in different projections of the feature space, the panels below present the diagonal 2-dimensional kernel-density estimates and the panels on the diagonal display 1-dimensional kernel-density estimates. The locations of SN 2021yfj and Type Ib/Ic SNe are highlighted in all 2-dimensional projections. SN 2021yfj’s light curve shares similarities with interaction-powered SNe Ib/Ic: a fast rise and a high peak luminosity. However, it sustains a high luminosity for a significantly longer period of time, which is uncommon for interaction-powered SESNe but comparable to regular supernovae. The combination of short rise and long duration places SN 2021yfj in a sparsely populated area of the light-curve parameter space.



**Extended Material Fig. 5: Fits of the light curve of SN 2021fj with models of three different powering mechanisms.** The panels in the upper half show the results using magnetar and nickel models in the software package `Redback` [55]. The bottom half shows a fit to the bolometric light curve using a CSM interaction model and the software package `CHIPS` [29, 30]. The CSM model can describe the observations. The mismatch between the observed and predicted rise can likely be mitigated with more complex CSM geometries and CSM density profiles than the ones considered here. The magnetar and nickel models can be excluded as the primary source of energy. The models do not simultaneously capture the rise, peak luminosity and peak time, and decline. Furthermore, the magnetar fit has an unphysically low opacity, and the nickel model requires an unphysically large nickel fraction. For illustration purposes, we only show the results in three filters. Details about the modelling are provided in the *Extended Material Light-Curve Modelling*. Non-detections are displayed as ‘▼’.



**Extended Material Fig. 6: Comparison of the light curves and blackbody properties of SN 2021yfj with those of other interaction-powered SESNe and the Type Ic SN 2020oi.** Compared to examples of interaction-powered SESN as well as the nickel-powered SN 2020oi, SN 2021yfj has a bright peak luminosity and a fast rise. Its blackbody radius and temperature evolve slowly in time compared to SNe Icn. This gradual evolution is reminiscent of some SNe IIn that are embedded in an optically thick CSM [e.g., 56], whereas the rapid evolution of Type Icn events suggests a CSM that is significantly less optically thick (*Methods Section Bolometric Light Curve*). The vertical dotted line in each panel indicates the date of the last nondetection of SN 2021yfj. The statistical uncertainties at the  $1\sigma$  confidence level are indicated as vertical error bars in the left panel and as bands in all other panels. Non-detections are displayed as ‘▼’.



**Extended Material Fig. 7: The properties of SN 2021yfj’s host galaxy.** *Left:* The SN position, marked by the crosshair, is located  $\sim 1.2$  kpc south from the centre of its star-forming dwarf host galaxy ( $M_r^{\text{host}} \approx -18.1$  mag). *Right:* The host of SN 2021yfj is a regular star-forming galaxy, demonstrated by its location with respect to the main sequence of star-forming galaxies (grey-shaded band, [57]). The properties are also consistent with hosts of core-collapse supernovae from the Palomar Transient Factory [58] (grey contours indicate the region encircling 68, 90, and 95%), including interaction-powered SESNe (Type Ibn and Icn SNe). The properties of all hosts were inferred from photometry using the software package Prospector [59]. The statistical uncertainties at the  $1\sigma$  confidence level are indicated.

**Extended Material Table 1:** The extension of the SN classification scheme after the discovery of SN 2021yfj.

Ejecta composition	CSM composition	SN Type	SN Type[27]
H	H	SN IIn	SN 0 i0
He	He, (H)	SN Ibn	SN 1 i1
C/O	C/O	SN Icn	SN 2 i2
O/Ne/Mg	O/Ne/Mg	SN Idn	SN 3 i3
<b>O/Si/S</b>	<b>O/Si/S</b>	<b>SN Ien</b>	<b>SN 4 i4</b>

The SN classification scheme from Ref. [27] (last column) is a progression of the traditional system (second last column). The first number is the spectroscopic classifier of the ejecta composition: 0 = strong H features; 1 = strong He features but no H; 2 = strong C and O but no H and He; 3 = strong O, Ne, Mg, but no C, He, H; and 4 = strong Si, S, O but no Mg, Ne, He and H. The tag “i” stands for interaction followed by the composition of the material with which the SN interacts: 0 = strong H features, etc. The value of ejecta and CSM composition can take fractional values to indicate transitional objects. The rows marked in grey are the new SN classes. SN 2021yfj belongs to the hitherto unknown class of Type Ien SNe (bold).



# Methods

## Discovery

SN 2021yfj, located at  $\alpha = 01^{\text{h}}37^{\text{m}}46^{\text{s}}.171$  and  $\delta = -01^{\circ}15'17''.78$  [J2000.0], was discovered by the public ZTF Northern Sky Survey as ZTF21abzbmhz at 09:56 (UTC dates are used throughout this paper) on 7 September 2021 with an apparent magnitude of  $r = 20.82 \pm 0.30$  mag, about 1.7 rest-frame days after the last nondetection [18]. The ZTF image-processing pipeline [60] generated an alert [61] based on image subtraction [62] with respect to a reference image. The alert was picked up by our custom “infant supernovae” filter [21, 63] running on the ZTF Fritz Marshal system [64, 65]. It was identified by a duty astronomer, and follow-up observations were triggered using our standard methodology [21, 66]. The ALerCE broker [67] team independently discovered ZTF21abzbmhz in the ZTF alert stream. They were also the first to report ZTF21abzbmhz to the IAU Transient Name Server<sup>1</sup> (TNS) [18]. ZTF21abzbmhz was allocated the name 2021yfj on 7 September 2021. Later detections were reported by the Asteroid Terrestrial-impact Last Alert System (ATLAS; [48]) survey on 12 September 2021 (internal name: ATLAS21bipz) and the Pan-STARRS Survey for Transients (PS; [68]) on 5 October 2021 (internal name: PS21ktg). On 3 September 2024, 2021yfj was designated the name SN 2021yfj [69, 70]. Unless stated otherwise, all times reported in this paper are with respect to the first detection and in the rest frame.

## Distance

The Keck spectrum from day 1 shows emission lines from hydrogen, oxygen and sulphur, produced by the ionised gas in the star-forming regions in the host galaxy, at a common redshift of  $z = 0.1386$ . We refine redshift with the higher-resolution spectra obtained with X-shooter at the VLT. These spectra also show emission lines from hydrogen and oxygen. Averaging over all epochs, we measure a redshift of  $z = 0.13865 \pm 0.00004$ . This is consistent with the redshift inferred from narrow absorption lines from Mg I  $\lambda$  2852 and Mg II  $\lambda\lambda$  2796, 2803 from the host ISM, detected in the X-shooter spectra up to 6.1 days after discovery, and the redshift inferred from the host emission lines detected in the Keck spectra at days 128.1 and 132.5. We use the redshift of  $z = 0.13865$  as the SN redshift throughout the paper. The redshift translates to a luminosity distance of 676.4 Mpc and a distance modulus of 39.15 mag using a flat  $\Lambda$ CDM cosmology with  $H_0 = 67.7 \text{ km s}^{-1} \text{ Mpc}^{-1}$ ,  $\Omega_{\text{m}} = 0.31$ , and  $\Omega_{\Lambda} = 0.69$  [23], which we use throughout the paper.

## Pre-explosion Limits

The ZTF survey started monitoring the SN field  $\sim 3.2$  yr before its explosion. We search the archival ZTF data for pre-SN outbursts following the methods described by Ref. [71]. We download IPAC difference images and compute the forced-photometry light curve at the SN position. After quality cuts, we are left with 612 pre-SN observations (74 points discarded) on 295 different nights in the ZTF  $g$ ,  $r$ , and  $i$  bands. We apply a baseline correction to ensure that the pre-SN light curve is centred around zero flux. The error bars are sufficiently large to account for the scatter of the pre-SN light curve and no upscaling of the statistical errors is required. We search for significant detections in unbinned and binned observations. Since the durations of the pre-explosion outbursts are unknown, we try seven different bin sizes between 1 and 90 days. We do not obtain  $5\sigma$  detections for any of the searches. For week-long bins, the median limiting magnitude is  $M > -18.8$  mag in  $g$  and  $r$  and  $M > -19.5$  mag in  $i$ . We can exclude outbursts that are brighter than those limits 50 (40) weeks before the explosion in  $r$  ( $g$ ). These limits are  $\gtrsim 1$  mag brighter than the most luminous precursors known [71], and hence do not pose meaningful limits on the outburst activity of SN 2021yfj’s progenitor shortly before the explosion.

## Light-Curve Properties

The first detection is recorded at 09:56 on 7 September 2021, about 1.7 rest-frame days after the last nondetection. At the time of the discovery, SN 2021yfj is very faint,  $r = 20.73 \pm 0.30$  mag [Milky Way (MW)-extinction corrected], but already luminous,  $-18.3$  mag, owing to its large distance (*Extended Material Distance*). It reaches its peak brightness in 2.3 and 5.8 rest-frame days in the  $g$  and  $r$  band, respectively. The MW-extinction corrected peak apparent magnitudes are  $m_g \sim 19.5 \pm 0.1$  mag and

---

<sup>1</sup><https://wis-tns.weizmann.ac.il/object/2021yfj>

$m_r \sim 19.7 \pm 0.1$  mag and translate to MW-extinction corrected,  $K$ -corrected [72] absolute magnitudes of  $M_g = -19.4 \pm 0.1$  mag and  $M_r = -19.1 \pm 0.1$  mag. At the peak of the  $g$ -band light curve, SN 2021y fj has a blue  $g - r$  colour of  $\sim -0.3$  mag,  $K$ -corrected and corrected for MW extinction. The high absolute magnitude at the time of discovery precludes estimating the explosion time as is commonly done for infant SNe (e.g., [19, 21, 73]).

To put SN 2021y fj in the context of other SN classes, we also compute the rise time from 50% peak flux and how long the brightness stayed above 50% of the peak flux in the  $g$  band. We measure a rise time of 3 days and a duration of 21.7 days. Both measurements have an uncertainty on the order of a few days. For comparison, we choose an extended sample of extragalactic transients from the ongoing ZTF Bright Transient Survey. We apply the following selection criteria: (i) no active galactic nuclei (AGNs), (ii) the passing of the BTS data-quality cuts presented in Ref. [45], (iii) well-sampled  $g$  and  $r$  light curves before, around, and after maximum brightness, (iv) a peak magnitude of  $< 19$  in  $g$  and  $r$  before MW-extinction correction, (v) a well-measured rise and decline timescale in both bands, (vi) a spectroscopic classification, and (vii) redshift information from either catalogues or the transient spectrum. In total, 4032 transients fulfil these criteria. The vast majority are Type Ia SNe (3178 objects, 79%; e.g., [74]) and Type II SNe (425 objects, 11%; e.g., [75]). The remaining 10% are other types of core-collapse supernovae (407 objects; e.g., [26, 27]), tidal disruption events (16 objects; e.g., [76]), intermediate luminosity red transients (3 objects; e.g., [77]), fast blue optical transients (1 object; e.g., [78]), gap transients (1 object; e.g., [79]) and luminous red novae (1 object; e.g., [80]). Among those objects, 22 objects are interaction-powered SESNe (Ibn: 20; Icn: 2). Their light curve properties (rise-time, duration, absolute peak magnitude and  $g - r$  colour at peak) are computed following Ref. [45]. This comparison sample and SN 2021y fj are shown in a 4-dimensional corner plot in the *Extended Material Figure 4*. Relative to the bulk population of SNe, the fast rise of SN 2021y fj ( $\sim 3$  days) represents its most extreme property. This, plus its relatively blue colour at peak ( $g - r \approx -0.3$  mag) and moderately high luminosity ( $M_g \approx -19.6$  mag) is largely consistent with the known population of SNe Ibn/Icn. Relative to the class of interacting SESNe, SN 2021y fj, however, stands out for its long duration ( $\sim 22$  days). In sum, aside from the short rise, SN 2021y fj has a light curve that is largely consistent with the general properties of Type Ia SNe and regular core-collapse supernovae.

To quantify the peculiarity of the photometric evolution of SN 2021y fj, we apply the Isolation Forest anomaly detection algorithm [81] to determine whether SN 2021y fj can be considered an outlier relative to other BTS sources. Briefly, an Isolation Forest builds a collection of decision trees and isolates individual sources by selecting a split point at random for a randomly selected feature within the feature space (4D as shown in the *Extended Material Figure 4*). Rare sources are, on average, isolated with fewer branch splittings within a tree than more common sources. Using the `scikit-learn` implementation of Isolation Forest [82] with the default settings, we train the forest on the 4032 BTS sources. We then apply the forest to SN 2021y fj and find that not only is it not an outlier, but also that  $\approx 15\%$  of the BTS sources are more “rare” than SN 2021y fj in the 4D light-curve property feature space.

## Bolometric Light Curve

Following the procedure outlined in Refs. [83, 84], we compute the bolometric light curve over the wavelength range from 1,800 to 7,850 Å (rest-frame), defined by the wavelength range of our photometric campaign from  $w2$  to  $z$  band. *Figure 3* shows the final bolometric light curve in black. A tabulated version is provided in the *Supplementary Material Table 7*.

The solid black line in *Figure 3* shows the time interval of the bolometric light curve with the best spectral coverage. The blue  $w2 - r$  colour of  $0.2 \pm 0.1$  mag at 1.5 days after the discovery of SN 2021y fj points to a substantial contribution from the far UV. Linearly extrapolating the observed spectral energy distribution (SED) to shorter wavelengths yields a missing far-UV fraction of  $39^{+10}_{-8}\%$  and  $22^{+10}_{-7}\%$  at day 1.5 and day 19.7, respectively. The missing flux contribution beyond  $1 \mu\text{m}$  is small. Fitting the observed SEDs from  $w2$  to  $z$  or from  $u$  to  $z$  yields a contribution of  $\sim 5\%$  between 1 and  $10 \mu\text{m}$  during the same time interval. The dark-grey curve in the *Extended Material Figure 3* shows the bolometric light curve, including the two missing flux fractions. Other epochs have less well-observed SEDs, and we use the data between day 1.5 and day 19.7 to estimate bolometric corrections. The rising light curve was only observed in the  $g$  and  $r$  bands. This wavelength interval accounts for 15% of the bolometric flux at day 1.5. Since SN ejecta cool with time, a constant bolometric correction will progressively underestimate the true bolometric flux toward earlier epochs. The fading light curve between days 19.7 and 32 was monitored from the  $u$  to  $i$  bands and in  $gri$  between days 32.0 and 34.8. Similar to the data at the previous time

interval, we compute bolometric corrections. The bolometric light curve of these time intervals is shown as dashed lines in the *Extended Material Figure 3*. At  $> 34.8$  days after discovery, SN 2021yjf is only detected in the  $g$  band. We omit these data in the bolometric light curve.

Integrating the entire light curve yields a radiated energy of  $0.6 \times 10^{50}$  erg. Including the missing far-UV and IR contributions increases the radiated energy by a factor of  $\sim 2$ . Both values are comparable to those of other interaction-powered SESNe, such as SNe 2019hgp (Icn,  $E_{\text{rad}} \approx 10^{50}$  erg; [13]), 2020bqj (Ibn,  $E_{\text{rad}} \approx 10^{50}$  erg; [85]), and 2021csp (Icn,  $E_{\text{rad}} \approx 10^{50}$  erg; [14]). Up to day 11.1, the spectra show a blackbody-like continuum with superimposed narrow emission lines but no broad metal absorption lines from the SN ejecta (*Supplementary Material Spectroscopic Evolution*). Fitting the photometry from 2,000 to 10,000 Å (observer frame) with the Planck function yields a temperature of  $\sim 16,000$  K at day 1.5 that gradually decreases to  $\sim 12,000$  K in  $\sim 3$  weeks and a radius that remains constant at  $\sim 10^{15}$  cm. The slow evolution of the bolometric light curve and the blackbody photosphere stand out compared to those of the well-observed interaction-powered SESNe 2010al, 2019hpg, and 2021csp (*Extended Material Figure 3*). The bolometric flux of SN 2021yjf decreases by less than 0.2 dex during the first two weeks since discovery, whereas the bolometric flux of the two Type Icn SNe faded by 1.0–1.2 dex and SN 2010al grew even brighter. The reasons for this are that SN 2021yjf’s photosphere remains at  $\sim 10^{15}$  cm at all times and merely gradually cools. Such an evolution has been observed in SNe IIn and was interpreted as the photosphere being located in the unshocked, optically thick CSM [56, 86]. In contrast to that, the photosphere of the Type Icn SNe 2019hgp and 2021csp undergoes a ballistic expansion, which points to a more optically thin CSM and, hence, a rapid decrease of the bolometric flux.

## Light-Curve Modelling

We model the multiband light curve with two distinct powering mechanisms using the open-source Bayesian inference software package `Redback` [55]: (i) radioactive decay of  $^{56}\text{Ni}$  [87] and (ii) spin-down of a rapidly spinning, highly magnetised neutron star (magnetar; [88]) utilising the generalised magnetar model by Ref. [89]. The two models include a component to account for the loss of  $\gamma$ -ray trapping at late times [90], which can increase the decline rate. Furthermore, we assume a Gaussian likelihood function, and we infer the model parameters with the `nessai` [91–93] sampler implemented in `Bilby` [94, 95]. The priors and marginalised posteriors of each model parameter are shown in the *Supplementary Material Table 8*.

The upper panels of the *Extended Material Figure 5* show fits with the two magnetar and nickel models in three different bands. Both models are inadequate to describe the observations. The models are not able to fit the rise, peak and decline simultaneously. Furthermore, the magnetar model predicts an unphysically low opacity of  $\kappa \approx 0.01 \text{ cm}^2 \text{ g}^{-1}$ , and the nickel requires an unphysically high nickel fraction of almost 100%. Therefore, we reject these two powering mechanisms as the primary source of energy.

Motivated by the lines of evidence for CSM interaction [*Methods Sections Spectroscopic Evolution and Comparison With Interaction-powered SESNe*], we model the bolometric light curve using the open-source code `CHIPS`<sup>2</sup> [29, 30]. The code uses hydrodynamical calculations, together with radiative transfer, to calculate bolometric light curves powered by SN ejecta colliding with a dense CSM of an arbitrary density profile. We consider homologously expanding ejecta with a density profile [96]

$$\rho_{\text{ej}}(r, t) = \begin{cases} t^{-3} [r/(gt)]^{-n} & (r/t > v_t), \\ t^{-3} (v_t/g)^{-n} [r/(tv_t)]^{-\delta} & (r/t < v_t), \end{cases}$$

where  $n = 10$  and  $\delta = 1$ , commonly adopted for explosions for SESN progenitors. The constants  $g$  and  $v_t$  relate to the ejecta mass  $M_{\text{ej}}$  and energy  $E_{\text{ej}}$  as [97]

$$g = \left\{ \frac{1}{4\pi(n-\delta)} \frac{[2(5-\delta)(n-5)E_{\text{ej}}]^{(n-3)/2}}{[(3-\delta)(n-3)M_{\text{ej}}]^{(n-5)/2}} \right\}^{1/n}, \quad v_t = \left[ \frac{2(5-\delta)(n-5)E_{\text{ej}}}{(3-\delta)(n-3)M_{\text{ej}}} \right]^{1/2}.$$

---

<sup>2</sup><https://github.com/DTsuna/CHIPS>

For the CSM density profile, we adopt a double power law, characterised by a shallow inner core and a steep drop generally found for simulations of envelope eruption [96, 98, 99],

$$\rho_{\text{CSM}}(r) = \hat{\rho}_{\text{CSM}} \left[ \frac{(r/r_{\text{CSM}})^{n_{\text{in}}/y} + (r/r_{\text{CSM}})^{n_{\text{out}}/y}}{2} \right]^{-y},$$

where  $r_{\text{CSM}}$  and  $\hat{\rho}_{\text{CSM}}$  set the radius and density at the transition of the two power laws, respectively. The remaining parameters  $n_{\text{in}}$  ( $\approx 0$ –3),  $n_{\text{out}}$  ( $\approx 10$ –12), and  $y$  ( $\approx 2$ –4.5) are set by the envelope structure as well as the detailed hydrodynamics of the mass loss. However, the overall light-curve morphology is sensitive only to  $n_{\text{in}}$ . We fix the other two as  $n_{\text{out}} = 10$  (as adopted in the *Methods Section Spectral Modelling*) and  $y = 2$ , inferred from simulations of partial envelope ejections from stripped progenitors [100]. CHIPS requires opacity tables for the CSM, which depend on its uncertain abundances. The spectra favour an O-dominant composition with enhanced Si/S/Ar and some He (*Methods Sections Spectroscopic Evolution, Hydrogen and Helium Content, and Spectral Modelling*). To reproduce this, we take the abundance of the surface of a stripped helium-poor stellar model with an initial mass of  $29 M_{\odot}$  available in CHIPS [30], and enhance the Si, S, and Ar mass fractions to those inferred from the *Methods Section Spectral Modelling* with carbon correspondingly reduced. The mass fractions adopted are 0.0081 (helium), 0.2041 (carbon), 0.6805 (oxygen), 0.0130 (neon), 0.0027 (magnesium), 0.05 (silicon), 0.03 (sulfur), 0.01 (argon), and small contributions of  $< 0.001$  for heavier metals. We use the Rosseland and Planck mean opacity tables for this composition, generated with TOPS [101]. While the adopted abundance may not exactly reflect that of the CSM, the bolometric light curves mostly depend on the dynamics of the interaction and much less on the composition details. We adopt a homologous CSM flow ( $v \propto r$ ) as in the *Methods Section Spectral Modelling* and set the constant of proportionality to the CSM velocity of  $2,000 \text{ km s}^{-1}$  at  $r = r_{\text{CSM}}$ , as observed in the early spectra (*Methods Section Spectroscopic Evolution*).

A successful fit to the bolometric light curve is shown in the bottom panel of *Extended Material Figure 5*, with the fitting parameters shown in *Supplementary Material Table 9*. We find that in order to reproduce the bolometric light curve one needs (i) a moderately large explosion energy ( $\sim 2 \times 10^{51}$  erg) and CSM mass ( $M_{\text{CSM}} \gtrsim 1 M_{\odot}$ , with the lower limit being the estimated mass of the CSM swept up by the shock at day 30) for the long bright peak, (ii) a shallow ( $n_{\text{in}} \approx 1$ ), extended ( $r_{\text{CSM}} \approx 5 \times 10^{15}$  cm) inner CSM profile for the slow decline (see, e.g., [97]), and (iii) a large  $M_{\text{ej}}$  ( $\gtrsim M_{\text{CSM}}$ ) so that the interaction power does not sharply decay owing to significant ejecta deceleration by the CSM. The inferred high masses and energy for the ejecta and CSM are within the possible range for successive mass ejections in pulsational pair instability (PPI) models [9, 36–38]. A pre-SN mass eruption in a lower-mass star cannot be ruled out, although a mechanism to eject such a large mass is less clear (*Methods Section Progenitor Scenarios*).

## X-ray Emission

The interaction of the SN ejecta with CSM and heating of the SN ejecta by a central engine (e.g., magnetar or black hole) can produce thermal X-ray emission [102, 103]. SN 2021yfr was not detected in our *Swift*/XRT observations (*Supplementary Material Table 4*). The inferred upper limits between  $10^{42}$  and a few  $10^{43} \text{ erg s}^{-1}$  (*Supplementary Material Table 4*) are comparable to the absorption-corrected luminosities of the X-ray brightest SNe [104–106], and thus do not place strong constraints on the lack of X-ray emission.

## Spectroscopic Evolution

*Extended Material Figure 1* shows the spectral evolution from the rest-frame near-UV to near-IR from 1 to 50 days after the SN discovery. The spectra up to day 11 are characterised by a cooling blackbody (from  $\sim 22,000$  to  $\sim 15,000$  K; *Figure 3*) with superimposed narrow emission lines (width:  $\sim 2,000 \text{ km s}^{-1}$ , *Extended Material Figure 2*). Following Ref. [107], we use the atomic spectra database from the National Institute of Standards and Technology (NIST; [108]) for the line identifications. We included all elements up to mass number 18 (argon) and created two ranked line lists for each ion sorted by (i) the relative line intensity, and (ii) the Einstein coefficient for spontaneous emission. We identify most lines as transitions from S III–IV, Si III–IV, and Ar III, and a very small minority of lines as transitions from Mg II, C III, and He I (*Figure 1, Extended Material Figure 3, Supplementary Material Table 1*).

The Si III-IV, S III-IV, and Ar III are visible for  $\lesssim 6$  days (i.e.,  $\approx 4$  days after the  $g$ -band maximum). As the bolometric luminosity (a proxy of the CSM interaction strength) and the blackbody temperature decrease, the highly-ionised species vanish, and the lines from singly ionised silicon and sulphur emerge. Between days 11 and 20, the spectrum transforms from a blackbody with narrow P Cygni lines to a blue pseudocontinuum, akin to those of interaction-powered SESNe [13, 14, 109], with superimposed intermediate (width: a few  $1,000 \text{ km s}^{-1}$ ) emission lines from neutral and low-ionisation silicon, sulphur, helium, magnesium, and oxygen.

The emission features in the early spectra are visible as either pure emission lines or P Cygni lines (examples shown in the *Extended Material Figure 2*). P Cygni lines can be produced in the expanding SN ejecta, in an expanding shell of gas expelled by the progenitor before the explosion, or in a stellar wind. The absorption minima of the P Cygni profiles are at  $\sim 1,500 \text{ km s}^{-1}$  and the blue edge of the absorption component is at  $\lesssim 3,000 \text{ km s}^{-1}$  (best seen in the isolated Mg II  $\lambda\lambda 2796, 2803$  doublet). These velocities are significantly lower than those of typical SN ejecta (e.g.,  $\sim 10,000 \text{ km s}^{-1}$ ; [24]). Instead, they are comparable to those of Wolf-Rayet stars [10] and the CSM velocities of interaction-powered SESNe [13, 14], meaning that SN 2021yfj’s ejecta interact with a fast-moving wind or shell of material that is rich in silicon and sulphur.

## Hydrogen and Helium Content

Hydrogen and helium constitute most of the baryonic matter in the Universe [110], and both elements play crucial roles in SN explosion and progenitor models [5]. Hydrogen has strong features at 4,861 and 6,563 Å [108]. Throughout the evolution of SN 2021yfj, we detect no hydrogen, neither in absorption nor emission. The blackbody temperature of SN 2021yfj is similar to that of H-rich Type II SNe (e.g., [111]); therefore, SN 2021yfj’s progenitor must have lost its hydrogen envelope well before the SN explosion. He I has its strongest optical transitions at 3,889, 4,471, 5,876, 6,678, and 7,065 Å. The first high-resolution spectrum, obtained at 1.6 days after discovery, (*Extended Material Figure 3*) shows well-defined emission lines at 3,889 and 5,876 Å; the 7,065 Å line is also detected but it is fainter than the 3,889 and 5,876 Å lines. The intrinsically weak He I line at 6,678 Å is not detected, though it is redshifted to the Telluric A band (*Extended Material Figure 3*). At the location of the 4,471 Å line there is a broad emission complex that is likely due to multiple species, meaning we cannot reliably determine whether a He I component exists at that wavelength.

Using the method of Ref. [107], we find that 3,889 and 5,876 Å are expected to be the strongest lines within the wavelength range we consider [108]. A comparison with an early spectrum of the prototypical He-dominated Type Ibn SN 2006jc [112] indicates that this event shows only the 3,889 and 5,876 Å lines at early times, further supporting the presence of He I in the spectrum of SN 2021yfj. The similarity between SN 2021yfj and SN 2006jc is maintained during later phases (*Figure 2*), where the broader He I lines at 5,876 Å and 7,065 Å are most prominent in the spectra of both SNe [12, 112]. We also detect an emission line at 10,830 Å at early and late times (*Extended Material Figures 3, 1*), where He I also has a strong transition. At late times, the 5,876-Å feature of SN 2021yfj reveals time-variable shoulders due to the contribution from singly-ionised silicon and sulphur (*Extended Material Figure 2*).

Therefore, we conclude that the spectroscopic data provide evidence for the existence of helium within the emitting material throughout the SN evolution.

## Comparison With Interaction-powered SESNe

To understand the peculiarity of SN 2021yfj, we compare its spectral evolution to that of other interaction-powered SESNe. We chose SNe 2006jc and 2010al (as archetypes of the Type Ibn class; [12, 20, 113]), and SNe 2019hgp and 2021csp (as archetypes of the Type Icn class; [13, 14]). SNe 2019hgp and 2021csp were detected within  $< 2$  days of their explosion dates, and spectra were acquired within hours after their discovery, offering an excellent opportunity to search for silicon, sulphur, and argon in their earliest spectra.

*Figure 2* shows snapshots of the spectral evolution before peak light (top), at maximum (centre), and more than one month after peak (bottom). The different SN classes evolve similarly. Up to the time of maximum light, the spectra are characterised by a thermal spectrum cooling from a few 10,000 K to 10,000–15,000 K and a series of narrow emission lines [full width at half-maximum intensity (FWHM)  $< 1000 \text{ km s}^{-1}$ ]. Well after maximum brightness, a blue pseudocontinuum develops, produced by a forest of

iron emission lines in the CSM, and a small number of emission lines with a FWHM of several  $1000 \text{ km s}^{-1}$ . Depending on the elemental composition of the CSM, different emission lines are visible: Type Ibn – helium (primarily), hydrogen, carbon, and oxygen; Type Icn – carbon, neon, oxygen (primarily) and helium; and SN 2021y fj– silicon, sulphur, argon (primarily) and helium. Furthermore, SNe 2010al and 2021csp show conspicuous emission from Ca II at  $8,500 \text{ \AA}$ . This feature is absent in SN 2021y fj, which is puzzling considering that argon, calcium, silicon, and sulphur are the ashes of the oxygen-burning phase (e.g., [7]).

In conclusion, the nondetection of silicon, sulphur, and argon in Type Ibn and Icn SNe and likewise the nondetection of hydrogen, nitrogen and oxygen and the weak presence of carbon and helium in SN 2021y fj, is not due to differences in the ionising radiation field, insufficient data quality, or the wavelength coverage. Instead, it reflects differences in the elemental composition of the CSM and, therefore, in the progenitor stars (e.g., [25]).

## A New Type of Supernova

The classification of SNe is fundamentally based on spectroscopy [26, 27]. The type of a SN is determined by the dominant spectroscopic features in its peak-light spectra: Type II SNe are dominated by hydrogen lines, Type Ib SNe by helium, and Type Ic SNe lack both hydrogen and helium. This sequence is assumed to reflect the amount of stripping of the progenitor stars, with those of SNe II having retained much of their initial hydrogen envelope, those of SNe Ib having lost the hydrogen layer but retaining the He-rich layer below, and those of SNe Ic having lost all or most of the He-rich layer. Adding the suffix “n” to the SN type is used to indicate the presence of relatively narrow spectral lines that arise from the SN progenitor having been surrounded by slowly-moving CSM whose composition reflects that of the outer stellar layer at the time of explosion or shortly prior. Thus, SNe IIn are surrounded by H-rich CSM, SNe Ibn have He-rich CSM, and SNe Icn have C/O-rich CSM. Following the theoretical shell structure of massive stars, one would expect that even further stripping would lead to the formation of stars whose outer layers are dominated by O/Ne/Mg and later O/Si/S, with natural designations of Type Id and Ie; events with narrow CSM lines would then be denoted by Idn and Ien (*Extended Material Table 1*). Our observations, presented in the *Supplementary Material Spectroscopic Evolution, Hydrogen and Helium Content, and Comparison With Interaction-powered SESNe*, suggest that SN 2021y fj is indeed the first example of a Type Ien SN [28]. This discovery also implies the existence of Type Id, Idn and Ie SNe. A late-time spectrum of the Type Ic SN 2021ocs [114] may indicate that its progenitor was more rich in O/Mg than the progenitors of other Type Ic SNe. SN 2021ocs could be Id or Ic/Id transitional SN. However, the evidence comes solely from a nebular spectrum, whereas SN classifications are based on their peak-light spectra. While it is too early to claim the detection of a Type Id SN, the discovery of SN 2021ocs is very intriguing.

## Spectral Modelling

Using the approach of Ref. [25], we simulate the early-time spectra of SN 2021y fj by adopting ejecta with a density profile of  $\rho \propto r^{-10}$ , a velocity of  $1000 \text{ km s}^{-1}$  at  $10^{15} \text{ cm}$  (together with a homologous flow, i.e.,  $r/v = \text{age} = 116 \text{ days}$ ), and a composition with the following mass fractions: 0.786 (oxygen), 0.1 (neon), 0.05 (silicon), 0.03 (sulphur), 0.01 (argon), 0.01 (magnesium), 0.001 (calcium), and solar abundance for iron, cobalt, and nickel. This composition is representative of the O/Si shell in a massive He-star model at the time of explosion, such as the he12 model used in Ref. [115]. The density is scaled so that the total Rosseland-mean optical depth of the ejecta is 40, assuming a mean opacity of  $0.1 \text{ cm}^2 \text{ g}^{-1}$ , roughly comparable with the results from the radiative-transfer calculation. This yields a total mass of  $3.24 M_{\odot}$ , which is quite substantial. Finally, a power of  $3 \times 10^{43} \text{ erg s}^{-1}$  is injected into the inner regions of these ejecta at  $v_{\text{deposition}} = 1000 \text{ km s}^{-1}$  over a characteristic scale of  $dv = 200 \text{ km s}^{-1}$ . The deposition profile goes as  $\exp[-(v - v_{\text{deposition}})^2 / dv^2]$ , and the volume-integrated power is normalised to  $3 \times 10^{43} \text{ erg s}^{-1}$ . Given these initial conditions, the radiative-transfer solution computes the temperature, ionisation, etc. We then compute steady-state, non-local thermodynamic equilibrium (NLTE) radiative-transfer models [25].

The results for the UV-optical spectrum are shown in *Figure 4*. The model spectra contain numerous lines of silicon and sulphur despite the relatively low abundance of a few 0.01, revealing that these elements have a strong absorption power, like iron, even for a modest abundance. Additional tests, in which we

raise the silicon and sulphur abundances until they reach values of 0.3–0.5, yield somewhat stronger silicon and sulphur lines, although not so much stronger, but progressively in tension with the observations. Decreasing the mass fraction below 1% gives weaker features, again in tension with observations. Hence, it seems that a mass fraction of a few 0.01 of silicon and sulphur is sufficient to explain the optical spectra of SN 2021yfj. These explorations remain somewhat short of the true complexity of SN 2021yfj. Indeed, no O-rich or Si-rich material in a massive star is also rich in helium, which is in tension with the presence of He I lines detected in SN 2021yfj (*Methods Section Hydrogen and Helium Content*). One way to accommodate this peculiarity is by invoking an asymmetric configuration in which He-rich material would be present in some “equatorial region” and O/Si-rich material interacts with that material, producing an interacting SN, with emission coming both from that He-rich CSM and the Si/O-rich ejecta. Further work is needed to investigate this aspect thoroughly.

## Host Galaxy

SN 2021yfj’s host galaxy was detected in several broad-band filters from the rest-frame UV to near-IR ( $m_r \approx 21$  mag; *Supplementary Material Table 5*). The left panel of the *Extended Material Figure 7* shows a false-colour image of the host galaxy, built with *gri* images from the DESI Legacy Imaging Surveys [116] and the software package STIFF [117] version 2.4.0. The SN explosion site is  $\sim 1.2$  kpc south of the galaxy centre. To infer the mass and star-formation rate of the host, we model the observed SED (*Supplementary Material Table 5*) with the software package *Prospector* [59] version 1.1.<sup>3</sup> We assume a Chabrier initial-mass function (IMF; [122]) and approximate the star-formation history (SFH) by a linearly increasing SFH at early times followed by an exponential decline at late times [functional form  $t \times \exp(-t/t_{1/e})$ , where  $t$  is the age of the SFH episode and  $t_{1/e}$  is the  $e$ -folding timescale]. To account for any reddening between the expected and the observed SED, we use the Calzetti attenuation model [123]. The priors of the model parameters are set identical to those used by Ref. [58]. The host galaxy has a stellar mass  $\log M_*/M_\odot = 8.9 \pm 0.2$ , a star-formation rate of  $0.07^{+0.10}_{-0.02} M_\odot \text{ yr}^{-1}$ , an age of  $4^{+4}_{-2}$  Gyr, and an attenuation of the stellar component of  $E(B - V) = 0.05^{+0.07}_{-0.03}$  mag ( $\chi^2/\text{n.o.f.} = 18.25/11$ , where n.o.f. is the number of photometric filters used in the SED modelling). The star-formation rate is comparable to typical star-forming galaxies of that stellar mass (grey band in *Extended Material Figure 7*; [57]). The mass and star-formation rate are also similar to the SN host galaxies from the Palomar Transient Factory (grey contours; [124–127]), including interaction-powered SESNe (colour-coded; the values of the SNe Icn were taken from Refs. [13, 14, 128]).

The SN spectra reveal emission lines from the ionised gas in H II regions along the line of sight, summarised in the *Supplementary Material Table 6*. Their luminosities and flux ratios allow us to determine the metallicity of the gas in the star-forming regions, the metal enrichment, and the level of attenuation. The MW-extinction corrected  $H\gamma/H\beta$  and  $H\delta/H\beta$  flux ratios are  $0.46 \pm 0.02$  and  $0.23 \pm 0.02$ , respectively. Both values are consistent with the theoretically predicted values of 0.47 and 0.26, assuming typical conditions of star-forming regions: Case B recombination, electron temperature of  $10^4$  K, and electron density of  $10^2 \text{ cm}^{-3}$  [129]. The nominal excess in the flux ratio translates to  $E_{\text{host}}(B - V) = 0.07 \pm 0.06$  mag, assuming the Calzetti attenuation model with  $R_V = 4.05$ . Owing to the small amount of attenuation and its large statistical measurement error, we assume negligible extinction for all SN properties. The  $H\alpha$  luminosity and the level of star formation are tightly correlated [130]. The attenuation-corrected star-formation rate is  $0.17 \pm 0.03 M_\odot \text{ yr}^{-1}$  using Ref. [130] and Ref. [131] to convert from the Salpeter IMF (assumed in Ref. 130) to the Chabrier IMF (assumed in our galaxy SED modelling). Both the attenuation and the star-formation rate are consistent with the values derived from the SED modelling. The metallicity of the star-forming region can be determined from the ratios between  $H\alpha$ ,  $H\beta$ ,  $[\text{N II}] \lambda 6584$ , and  $[\text{O III}] \lambda 5007$  [132]. Using this O3N2 diagnostic together with the parameterisation from Ref. [133], we infer a gas-phase metallicity of  $0.53 \pm 0.01$  solar, a normal value for a galaxy of that mass [134].

We note that SN 2021yfj exploded close to the centre of its host galaxy, and the slit covered a large fraction of the host galaxy. The properties reported above are, hence, representative of the SN explosion site and the entire galaxy.

---

<sup>3</sup>*Prospector* uses the Flexible Stellar Population Synthesis (FSPS) code [118] to generate the underlying physical model and *python-fsps* [119] to interface with FSPS in python. The FSPS code also accounts for the contribution from the diffuse gas based on the Cloudy models from [120]. We use the dynamic nested sampling package *dynesty* [121] to sample the posterior probability.

## Event Rate

The WISeREP archive contains  $> 400$  public spectra for  $> 70$  SNe Ibn/Icn. We examined all spectra to determine whether any of the objects showed narrow silicon or sulphur lines. None of the objects has spectra exhibiting silicon, sulphur, and argon lines. This reveals that SN 2021y fj is the first member of a previously unknown supernova class and that Type Icn SNe are an even rarer class of objects than the already rare Type Ibn and Icn SNe (SNe Ibn, 0.1–0.5%; SNe Icn, 0.005–0.05% of the total CCSN rate; [14]).

The nondetection of Type Icn SNe in the ZTF Bright Transient Survey allows us to place an upper limit on their volumetric rate. Figure 9 in Ref [45] shows the relationship between the volumetric rate as a function of peak absolute magnitude derived from the ZTF Bright Transient Survey. Using the same methodology together with the 6-year BTS sample and assuming that SNe Icn reach an absolute magnitude of  $< -19$  mag at peak, their volumetric rate is  $< 30 \text{ Gpc}^{-1} \text{ yr}^{-1}$  at 95% confidence (Poisson statistics), which is roughly  $< 1/1,000$  the rate of SNe Ib/c [46] and  $< 1/3,000$  of the total CCSN rate [45].

## Progenitor Scenarios

Knowing that a moderate amount of silicon and sulphur suffices to explain the features of the early-time spectra of SN 2021y fj, we now explore possible progenitor channels.

### A High-mass Massive Star

Massive stars can lose a substantial amount of their birth mass through stellar winds [135, 136], eruptions [136, 137], and interaction with a companion star [138, 139]. First, we focus on stars that have lost their entire hydrogen envelope, so-called He stars, with a pre-supernova mass between  $30$  and  $133 M_{\odot}$ . During the oxygen-burning phase of such a star,  $e^+e^-$  pairs are formed, reducing the radiation pressure that supports the star against gravitational collapse (so-called pair instability; [36–38]). As a result, implosive oxygen burning can produce enough energy to unbind a substantial amount of the stellar envelope. He cores above  $\gtrsim 64 M_{\odot}$  experience a single violent pulse that unbinds the entire star [140–144]. Less-massive stars can encounter pair instability a few times and eject shells of increasingly metal-rich CSM. The collisions of shells can produce luminous optical transients, so-called pulsational pair-instability SNe (PPISNe; [9, 145, 146]). The specific mass limits depend on the uncertain rate of the  $^{12}\text{C}(\alpha, \gamma)^{16}\text{O}$  reaction rate [147–149], but for reasonable choices, a qualitatively similar behaviour is observed in the transition region between PPISNe and PISNe, wherever it occurs. PPISN models usually do not produce shells that contain much silicon and sulphur. Usually, the outer layers of helium, carbon, oxygen, magnesium, and neon are ejected. In the transition between PPISN and PISN, the first pulse can eject an arbitrary amount of mass and expose the oxygen convective shell. This extensive convective shell encompasses much of the star and may be mildly enhanced in newly synthesised silicon.

Among the available PPISN models, the He60/61 model of Ref. [9] with a helium-core mass of  $60$ – $61 M_{\odot}$  is of particular interest. It has an oxygen convective shell with a composition similar to that of the he12 model whose predicted spectral features matched the observed ones at early times (*Methods Section Spectral Modelling*). In the He61 model, the first pulse ejects  $19 M_{\odot}$ , exposing the O/Ne shell. The remaining  $42 M_{\odot}$  are almost unbound, but eventually, the star contracts and reencounters pair instability. Enough nuclear fuel is left for a few final pulses that happen in rapid succession before the iron core directly collapses into a black hole. With each new pulse, a new shell (moving with a velocity of a few  $1,000 \text{ km s}^{-1}$ ) is enriched in increasingly heavier elements, and, eventually, material from the oxygen convective shell, which could be enhanced in silicon, can be expelled. The collisions between the shells (pulse 2 and later) can produce light curves with rise times as short as a few days, durations of several tens of days, and peak luminosities reaching a few  $10^{43} \text{ erg s}^{-1}$ . Collisions between the shells can radiate up to  $5 \times 10^{50} \text{ erg}$  and produce spectra that are dominated by interaction [9]. However, the exact properties are more uncertain. They are highly sensitive to the properties of the first pulse, the kinematics of the shells, the mass they carry, the time between the pulses, mixing processes, and details of the simulations [9, 39, 150, 151].

In the PPISN scenario, SN 2021y fj could be the product of a collision between the last shells ejected before the progenitor star collapsed to form a black hole. Qualitatively, the PPI model explains many of the observed properties, such as the wind velocity of  $3,000 \text{ km s}^{-1}$ , presence of silicon, sulphur, and argon



in the early spectra, interaction-dominated spectra throughout the entire evolution (*Methods Section Spectroscopic Evolution*), the rise time of 3 days, the peak luminosity of  $(3\text{--}5) \times 10^{43}$  erg s<sup>-1</sup>, and the radiated energy of  $(0.5\text{--}1) \times 10^{50}$  erg (*Methods Section Light-Curve Properties*). It could also provide a mechanism to strip a star to its oxygen convective shell. The host metallicity of  $\lesssim 0.5$  solar (*Methods Section Host Galaxy*) and low event rate of SN 2021yfj-like transients (*Methods Section Event Rate*) match further predictions of PPISN models.

The presence of helium (*Methods Section Hydrogen and Helium Content*) in the spectra of SN 2021yfj is puzzling. There was helium on the surface of the 61/62- $M_{\odot}$  models, but it was ejected about a thousand years before the explosion and now resides at  $\sim 10^{18}$  cm, maybe less if it collides with dense CSM. Since massive stars tend to live in binary systems, it may not be too unlikely to have a helium-star companion with a strong wind. All stars this massive have nearly the same lifetimes burning hydrogen and helium ( $3 \times 10^6$  and  $3 \times 10^5$  yr, respectively), so a coeval star could be in a similar stage of evolution.

## A Low-mass Massive Star

In the regime of less-massive He stars, a few scenarios could give rise to SN 2021yfj, as follows.

**Scenario A** — Helium stars with pre-supernova masses in the range 2.0 to 2.6  $M_{\odot}$  have a complex final evolution that is strongly influenced by electron degeneracy [152, 153]. To make a low-mass helium star, a close interacting binary is a necessary starting point. Both oxygen and silicon burning ignite far off centre in these stars, and the fusion propagates inward as “flames” bounding a molecular-weight inversion that might be unstable [152]. The stars also have unusually large radii ( $\sim 10^{13}$  cm) that they develop after core helium depletion. Some also experience strong, degenerate silicon flashes that, while energetically incapable of exploding the entire star, can eject all or part of the matter outside the silicon core. A relevant scenario would be (i) the silicon flash plus any residual binary interaction removes most of the matter external to the oxygen-burning shell; (ii) during the following months, the inwardly propagating flame powers a strong wind that ejects more silicon-rich matter; and (iii) a terminal iron-core collapse creates an outgoing shock with  $\sim 10^{50}$  erg. The bright supernova results from the terminal explosion interacting with the wind and ejected shell, as shown in Figure 14 of Ref. [153]. This could be a more common occurrence than a PPISN and does not require low metallicity or a high star-formation rate. Helium would also be present in the recently ejected matter. The difficulty is the many uncertainties surrounding the energy and timing of the silicon flash; the propagation, in more than one dimension (1D), of the flames; and the extent to which the flash and winds uncover silicon-rich material prior to the terminal explosion. We note that based on simulations by Ref. [25], the CSM around such low-mass stars is expected to consist mostly of helium, which leads to strong helium features throughout the entire evolution, inconsistent with observations of SN 2021yfj [*Extended Material Figure 3, 1*]. This channel might be ideal for Type Ibn SNe [25], but less so for SN 2021yfj.

**Scenario B** — Some massive stars produce jets during their terminal explosion [154, 155]. The appearance of Si/S material in the outer layer could be the result of a jetted explosion where jets lift and drag material from the stellar interior onto the outer layers. In this scenario, SN 2021yfj would have to be observed from a preferred direction close to on-axis. This might also produce a  $\gamma$ -ray flash as seen in long-duration GRBs, which are connected with the explosion of very massive stars. We found no  $\gamma$ -ray flash or an afterglow in the X-ray or the optical cospatial with SN 2021yfj within 2 days before the discovery of SN 2021yfj (*Supplementary Material High-Energy Observations*).

Considering SN 2021yfj’s moderately high redshift, an intrinsically weak  $\gamma$ -ray flash would likely have evaded detection with current  $\gamma$ -ray satellites [156, 157]. Furthermore, a baryon loading of as little as  $10^{-4} M_{\odot}$  is expected to stifle the formation of a relativistic jet [158], leading instead to the formation of a nonrelativistic outflow. An outflow should not only dredge up silicon and sulphur; it should also transport carbon, oxygen, and neon from the layers between the inner Si/S shell and the other He shell. However, strong lines from carbon, oxygen, and neon are absent in the spectra of SN 2021yfj.

## A Merger of Two Compact Objects

In the following, we explore whether silicon and sulphur could be formed on the surface of a white dwarf or possibly a neutron star. Simulations by Ref. [159] showed that helium burning at low densities

( $\sim 10^9 \text{ g cm}^{-3}$ ) and low temperatures ( $\sim 10^9 \text{ K}$ ) produces silicon and sulphur. Helium burning is an exothermal process, though. The temperature increase would cease the production silicon and sulphur and instead continue fusing the ashes to nickel [159]. The excess energy could be dissipated through the expansion of the gas. However, this would also skew the production toward heavier nuclei [159]. Cooling by emitting neutrinos is not possible since silicon and sulphur are stable against  $\beta$  decay in these conditions. Simulations of helium burning on the surface of C/O white dwarfs [160] revealed that the density on their surface is always  $\ll 10^9 \text{ g cm}^{-3}$ , making the production of silicon and sulphur subdominant to the more common elements, such as calcium, magnesium, and iron-group elements. We note, though, that helium burning on the surface of different types of compact objects (white dwarfs and neutron stars) is underexplored, and detailed simulations are needed.

## Acknowledgements

M. W. Coughlin acknowledges support from the U.S. National Science Foundation (NSF) with grants PHY-2308862 and PHY-2117997. A. V. Filippenko’s group at UC Berkeley is grateful for financial assistance from the Christopher R. Redlich Fund, Gary and Cynthia Bengier, Clark and Sharon Winslow, Alan Eustace (W.Z. is a Bengier-Winslow-Eustace Specialist in Astronomy), William Draper, Timothy and Melissa Draper, Briggs and Kathleen Wood, Sanford Robertson (T.G.B. is a Draper-Wood-Robertson Specialist in Astronomy), and many other donors. A. Gal-Yam’s research is supported by the ISF GW excellence centre, an IMOS space infrastructure grant and BSF/Transformative and GIF grants, as well as the André Deloro Institute for Space and Optics Research, the Center for Experimental Physics, a WIS-MIT Sagol grant, the Norman E Alexander Family M Foundation ULTRASAT Data Center Fund, and Yeda-Sela; A. Gal-Yam is the incumbent of the Arlyn Imberman Professorial Chair. N. Knežević was supported by the Ministry of Science, Technological Development and Innovation of the Republic of Serbia (MST-DIRS) through contract no. 451-03-66/2024-03/200002 made with the Astronomical Observatory (Belgrade) and contract no. 451-03-66/2024-03/200104 made with the Faculty of Mathematics at the University of Belgrade. R. Lunnan acknowledges support from the European Research Council (ERC) under the European Union’s Horizon Europe research and innovation programme (grant agreement 1010422). K. Maeda acknowledges support from the JSPS KAKENHI grant JP20H00174 and JP24H01810. A. A. Miller and S. Schulze are partially supported by LBNL Subcontract 7707915. N. Sarin acknowledges support from the Knut and Alice Wallenberg foundation through the “Gravity Meets Light” project. D. Tsuna is supported by the Sherman Fairchild Postdoctoral Fellowship at the California Institute of Technology. Y. Yang appreciates the generous financial support provided to the supernova group at U.C. Berkeley by Gary and Cynthia Bengier, Clark and Sharon Winslow, Sanford Robertson, and numerous other donors. We appreciate the excellent assistance of the staff at the various observatories where data were obtained. U.C. Berkeley undergraduate student Evelyn Liu is thanked for her effort in taking Lick/Nickel data.

Based in part on observations obtained with the 48-inch Samuel Oschin Telescope and the 60-inch Telescope (P60) at the Palomar Observatory as part of the Zwicky Transient Facility project. ZTF is supported by the U.S. NSF under grants AST-1440341 and AST-2034437, and a collaboration including current partners Caltech, IPAC, the Weizmann Institute of Science, the Oskar Klein Centre at Stockholm University, the University of Maryland, Deutsches Elektronen-Synchrotron and Humboldt University, the TANGO Consortium of Taiwan, the University of Wisconsin at Milwaukee, Trinity College Dublin, Lawrence Livermore National Laboratories, IN2P3, University of Warwick, Ruhr University Bochum, Northwestern University, and former partners the University of Washington, Los Alamos National Laboratories, and Lawrence Berkeley National Laboratories. Operations are conducted by COO, IPAC, and UW. ZTF access was supported by Northwestern University and the Center for Interdisciplinary Exploration and Research in Astrophysics (CIERA). The SED Machine on P60 is based upon work supported by NSF grant 1106171. Some of the data presented herein were obtained at Keck Observatory, which is a private 501(c)3 nonprofit organisation operated as a scientific partnership among the California Institute of Technology, the University of California, and the National Aeronautics and Space Administration. The Observatory was made possible by the generous financial support of the W. M. Keck Foundation. Based in part on observations collected at the European Organisation for Astronomical Research in the Southern Hemisphere under ESO programme(s) 105.20KC and 105.20PN. Data presented here were obtained in part with ALFOSC, which is provided by the Instituto de Astrofísica de Andalucía (IAA) under a joint agreement with the University of Copenhagen and NOT. KAIT and its ongoing operation at Lick Observatory were made possible by donations from Sun Microsystems, Inc., the Hewlett-Packard Company,

AutoScope Corporation, Lick Observatory, the U.S. NSF, the University of California, the Sylvia & Jim Katzman Foundation, and the TABASGO Foundation. A major upgrade of the Kast spectrograph on the Shane 3 m telescope at Lick Observatory was made possible through generous gifts from William and Marina Kast as well as the Heising-Simons Foundation. Research at Lick Observatory is partially supported by a generous gift from Google. Based on observations made with the Liverpool Telescope operated on the island of La Palma by Liverpool John Moores University in the Spanish Observatorio del Roque de los Muchachos of the Instituto de Astrofísica de Canarias with financial support from the UK Science and Technology Facilities Council. We acknowledge the use of public data from the *Swift* data archive.

## Author Contributions

Contributors are sorted alphabetically.

- **Observations and Data Reduction** — M. Bulla, R. Lunnan, S. Schulze (X-shooter), T. G. Brink, A. V. Filippenko, Y. Yang and W. Zheng (Keck, KAIT), K. Hinds and D. A. Perley (LT), S. Schulze and J. Sollerman (NOT), Y. Sharma and T. Sit (P200), R. Lunnan, D. A. Perley, Y. Sharma, and Y. Yao (Keck), S. Schulze (*Swift*), A. Gangopadhyay (bolometric light curve of SN 2020al), and K. Hinds and D. A. Perley (BTS catalogue)
- **Discoverer of the Si, S, Ar lines** — A. Gal-Yam
- **Analysis** — P. Chen, L. Dessart, A. Gal-Yam, I. Irani, N. Knežević, A. A. Miller, D. A. Perley, N. Sarin, S. Schulze, N. L. Strothjohann, D. Tsuna, and O. Yaron
- **Discussion and Interpretation** — All authors contributed to discussions and interpretation.
- **Paper Writing** — L. Dessart, A. V. Filippenko, A. Gal-Yam, A. A. Miller, S. Schulze, J. Sollerman, N. L. Strothjohann, D. Tsuna, and S. E. Woosley
- **ZTF Infant SN Programme 2018–2023** — R. J. Bruch, M. Bulla, P. Chen, S. Dhawan, A. Gal-Yam, I. Irani, S. Schulze, J. Sollerman, N. L. Strothjohann, Y. Yang, O. Yaron, and E. A. Zimmerman

## Data Availability

The reduced spectra and photometry of SN 2021yfy will be made available via the WISeREP archive and the journal webpage after the acceptance of the paper. Data from ESO, Keck, NOT, *Swift*, and ZTF can be obtained from their designated public data repositories.

## Code Availability

Much analysis for this paper has been undertaken with publicly available codes. The details required to reproduce the analysis are contained within the manuscript.

# Supplementary Material

## Observations and Data Reduction

### Photometry

**Zwicky Transient Facility** — The Zwicky Transient Facility (ZTF) uses the Samuel Oschin 48-inch (1.22 m) Schmidt telescope at Palomar Observatory on Mount Palomar (USA). It is equipped with a 47-square-degree camera [161] and monitors the entire northern hemisphere every 2–3 days in the  $g$  and  $r$  bands to a depth of  $\sim 20.7$  mag ( $5\sigma$ ; [16, 17]) as part of the public ZTF Northern Sky Survey [162]. We retrieved the host-subtracted photometry via the Infrared Processing and Analysis Center (IPAC) ZTF forced-photometry service [163]. This service uses the data-reduction techniques outlined in Ref. [60]. We cleaned and calibrated the data following Ref. [163].

**2.56 m Nordic Optical Telescope** — We obtained photometry in  $gri$  with the Alhambra Faint Object Spectrograph and Camera (ALFOSC)<sup>4</sup> on the 2.56 m Nordic Optical Telescope (NOT) at the Roque de los Muchachos Observatory on La Palma (Spain). To remove the host contribution, we obtained a final set of  $gri$  photometry in August/September 2022, after the SN had faded. We reduced the data with PyNOT<sup>5</sup> using standard techniques for CCD data processing and photometry. The world coordinate system was calibrated with the software package `astrometry.net` [164]. The host contribution was removed with custom image-subtraction and analysis software (K. Hinds, K. Taggart, et al., in prep.). The photometry was measured using point-spread-function (PSF) fitting techniques based on methods in Ref. [165].

**Palomar 60-inch telescope** — We acquired additional  $ugri$  photometry using the Rainbow Camera of the Spectral Energy Distribution Machine (SEDM; [166, 167]) on the robotic Palomar 60-inch (1.52 m) telescope (P60; [168]) at Palomar Observatory. The data were reduced using the data-reduction pipeline FPipe [165].

**0.76 m Katzman Automatic Imaging Telescope and 1 m Nickel Telescope** — We obtained photometry in  $BVRI$  and in the *Clear* band (close to the  $R$  band; [169]) with the 0.76 m Katzman Automatic Imaging Telescope (KAIT) at Lick Observatory on Mount Hamilton (USA) as a part of the Lick Observatory Supernova Search (LOSS; [170]). One additional epoch of photometry was also obtained with the 1 m Nickel telescope at Lick Observatory. We reduced images using a custom pipeline<sup>6</sup> detailed in Ref. [171]. We performed PSF photometry with the package DAOPHOT [172] from the IDL Astronomy User’s Library<sup>7</sup>.

**2 m Liverpool Telescope** — We acquired photometry in  $ugriz$  using the Infrared-Optical Imager (IO:O) on the robotic Liverpool Telescope (LT; [173]) at Roque de los Muchachos Observatory. Reduced images were downloaded from the LT archive and processed with custom image-subtraction and analysis software (K. Hinds, K. Taggart, et al., in prep.). Image stacking and alignment were performed using SWarp [174] where required. Image subtraction was performed using a pre-explosion reference image in the appropriate filter from the Panoramic Survey Telescope and Rapid Response System (Pan-STARRS) Data Release (DR) 1 [175] or Sloan Digital Sky Survey (SDSS) DR9 [176]. The photometry is measured using PSF fitting techniques based on methods in Ref. [165].

**Neil Gehrels Swift Observatory** — We submitted a target of opportunity request to use the 30 cm Ultraviolet/Optical Telescope (UVOT; [177]) aboard the *Neil Gehrels Swift Observatory* [178] to expand the wavelength coverage to the UV. Between January and February 2022, we obtained deep images in all filters to remove the host-galaxy contamination from the transient photometry. We coadded all sky exposures for a given epoch to boost the signal-to-noise ratio (S/N) using `uvotimsum` in HEASOFT<sup>8</sup> version 6.32.2. Afterward, we measured the brightness of SN 2021yfq with the *Swift* tool `uvotsource`. The source aperture had a radius of  $5''$ , while the background region had a significantly larger radius. To remove the host contribution in  $w2$ ,  $m2$ , and  $w1$  from the earlier epochs, we arithmetically subtracted the host flux from the early measurements when the SN was bright.

**Final photometry** — The datasets were calibrated against stars from the Sloan Digital Sky Survey (SDSS; e.g., P60, LT, NOT observations; [176]) and Pan-STARRS (e.g., ZTF; [60, 175, 179]), and internal zeropoints (*Swift*; [180]). Observations in similar but not identical filters (e.g., SDSS vs. ZTF filters) could

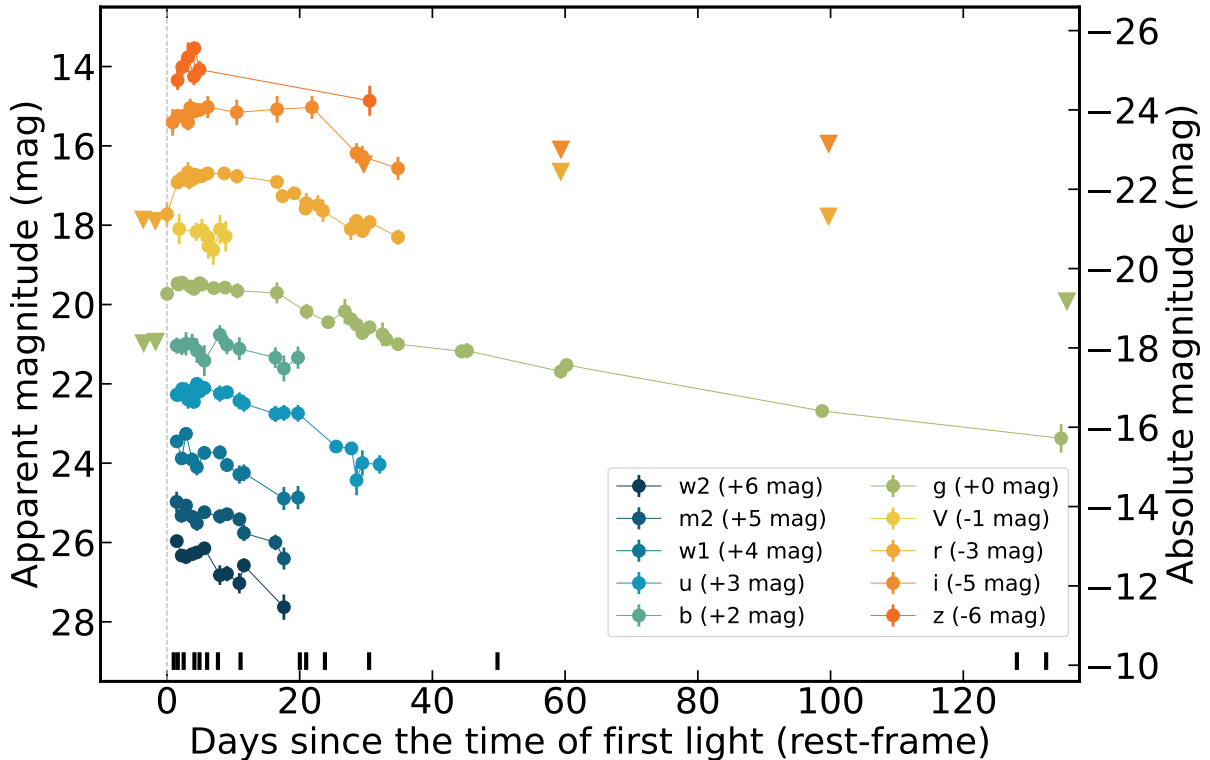
<sup>4</sup><http://www.not.iac.es/instruments/alfosc>

<sup>5</sup><https://github.com/jkrogager/PyNOT>

<sup>6</sup><https://github.com/benstahl92/LOSSPhotPipeline>

<sup>7</sup><http://idlastro.gsfc.nasa.gov>

<sup>8</sup><https://heasarc.gsfc.nasa.gov/docs/software/heasoft>



Supplementary Material Fig. 1: The multiband light curves of SN 2021y fj from 1,800 to 7,850 Å (rest frame) corrected for MW extinction. Vertical bars represent the epochs of spectroscopy. The absolute magnitude is computed with  $M = m - DM(z) + 2.5 \log(1 + z)$ , where  $DM$  is the distance modulus and  $z$  the redshift. Non-detections are displayed as ‘▼’.

introduce measurable, time-dependent colour terms [181]. Convolution spectra between days 1.0 and 49.8 with SDSS and ZTF filter response functions yielded differences in the filter systems between 0.01 and 0.07 mag. They were comparable to, if not smaller than, the measurement uncertainties. Owing to this, we merged the datasets without applying any colour terms.

The final photometric data are shown in the *Supplementary Material Figure 1* and the *Supplementary Material Table 2*. All measurements are reported in the AB system [182]. The measurements in the *Supplementary Material Table 2* are not corrected for Galactic extinction along the line of sight, but the Galactic extinction correction is applied to all photometric data shown in the figures and the derived properties. The MW extinction along the line of sight is  $E(B - V) = 0.03$  mag [183]. We assumed the Cardelli parameterisation of the MW extinction [184] and a total to selective extinction ratio of  $R_V = 3.1$ .

## Spectroscopy

We obtained 16 spectra with several 2–10 m-class telescopes. *Supplementary Material Table 3* shows the observing log. Details about the observations and the data reductions are provided below.

**10 m Keck Telescope** — We obtained 4 epochs with the Low-Resolution Imaging Spectrometer (LRIS; [185]) on the 10 m Keck I telescope at Maunakea (USA) between days 1.0 and 132.5. The first and the third epochs, acquired on 8 September 2021 (day 1) and 31 January 2022 (day 132.5), used the B600/4000 blue-side grism and the R400/8500 red-side grating, dichroic 5600, and a 1''-wide slit. For the second and fourth epochs (days 23.8 and 128.1), we utilised the B400/3400 blue-side grism and the R400/8500 red-side grating, dichroic 5600, and a 1''-wide slit. The integration times varied between 1,200 and 3,600 s depending on the epoch. To minimise slit losses caused by atmospheric dispersion [186], the spectra were acquired with the slit oriented at or near the parallactic angle. All spectra were reduced in a standard fashion with the data-reduction pipeline LPipe [187].

**8.2 m ESO Very Large Telescope** — We collected seven medium-resolution spectra with the X-shooter instrument [188] at the 8.2 m Very Large Telescope (VLT) at Paranal Observatory (Chile) between

9 September and 11 November 2021 (days 1.6 to 49.8). All observations were performed in nodding mode and with  $1''0/0''9/0''9$ -wide slits (UVB/VIS/NIR arm). Each spectrum covers the wavelength interval from 3,000 to 24,800 Å. The integration times varied between 2,880 and 4,400 s, depending on the arm (UVB/VIS/NIR) and phase. All observations were done with an atmospheric dispersion corrector to minimise any flux losses. The data were reduced following Ref. [189]. In brief, we first removed cosmic rays with the tool `astrocrappy`<sup>9</sup>, which is based on the cosmic-ray removal algorithm by Ref. [190]. Afterward, the data were processed with the X-shooter pipeline v3.3.5 and the ESO workflow engine `ESOReflex` [191, 192]. The UVB- and VIS-arm data were reduced in stare mode to boost the S/N. The individual rectified, wavelength- and flux-calibrated 2D spectra files were coadded using tools developed by J. Selsing<sup>10</sup>. The NIR data were reduced in nodding mode to ensure good sky-line subtraction. In the third step, we extracted the 1D spectra of each arm in a statistically optimal way using tools by J. Selsing. Finally, the wavelength calibration of all spectra was corrected for barycentric motion. The spectra of the individual arms were stitched by averaging the overlap regions.

**Palomar 200-inch Telescope** — We obtained one epoch with the Double Spectrograph (DBSP; [193]) on the Palomar 200 inch (5.1 m) telescope at Mount Palomar Observatory on 13 September 2021 (day 5.2). The observations were taken using the D-55 dichroic beam splitter, a blue grating with 600 lines  $\text{mm}^{-1}$  blazed at 4,000 Å, a red grating with 316 lines  $\text{mm}^{-1}$  blazed at 7,500 Å, and a  $1''5$ -wide slit. To minimise slit losses caused by atmospheric dispersion, the spectrum was acquired with the slit oriented at the parallactic angle. The data were reduced using the Python package `DBSP_DRP`<sup>11</sup> that is primarily based on `PyPeIt` [194, 195] and utilises common methods in optical spectroscopy.

**2.56 m Nordic Optical Telescope** — We collected 3 epochs of low-resolution spectroscopy with ALFOSC on the NOT between 7 January and 22 February 2019 (days 4.1 to 11.1). The spectra were obtained with grism #4 and either a  $1''0$ - or  $1''3$ -wide slit, depending on the weather conditions. To minimise slit losses caused by atmospheric dispersion, the spectra were acquired with the slit oriented at the parallactic angle. The data were reduced with `PyNOT` using standard techniques for CCD data processing and long-slit spectroscopy.

**Shane 3 m telescope** — We obtained one spectrum with the Kast double spectrograph<sup>12</sup> mounted on the Shane 3 m telescope at Lick Observatory on 11 September 2021 (day 3.5). We utilised a  $2''$ -wide slit, the 600/4310 grism in the blue, and the 300/7500 grating in the red. This instrument configuration has a combined wavelength range of  $\sim 3,500$ – $10,500$  Å. To minimise slit losses caused by atmospheric dispersion, the Kast spectrum was acquired with the slit oriented at or near the parallactic angle. The Kast data were reduced following standard techniques for CCD processing and spectrum extraction [196] utilising `IRAF` routines and custom `Python` and `IDL` codes<sup>13</sup>. Owing to the low quality of the Lick spectrum, it is not shown in any of the figures in the paper, but it can be downloaded from WISeREP like all other spectra.

**Flux calibration and host correction** — The flux calibration of all spectra was achieved with spectrophotometric standard stars observed during the same nights. We also tied the absolute flux scale to our multiband photometry. As the SN faded, the relative contribution from the host galaxy increased. To remove the host contribution, we used the X-shooter observation obtained at day 49.8, which also covered the host galaxy. The host was detected in the LRIS spectra from January/February 2022, too. While the continua of the three spectra were identical, the spectra differed in the relative amplitude of the emission lines due to the different resolving powers.

## High-Energy Observations

While monitoring SN 2021yfj with UVOT between day 1.5 and day 148.7, *Swift* also observed the field with its onboard X-ray telescope XRT between 0.3 and 10 keV in photon-counting mode [197]. We analysed these data with the online tools of the UK *Swift* team<sup>14</sup> that use the software package `HEASoft` version 6.26.1 and methods described in Refs. [198, 199]. SN 2021yfj evaded detection at all epochs. The median  $3\sigma$  count-rate limit of each observing block is  $6 \times 10^{-3} \text{ s}^{-1}$  (0.3–10 keV). Coadding all data pushes the  $3\sigma$  count-rate limits to  $0.6 \times 10^{-3} \text{ s}^{-1}$ . To convert the count-rate limits into a flux, we assume a power-law spectrum with a photon index<sup>15</sup> of  $\Gamma = 2$  and a Galactic neutral hydrogen

<sup>9</sup><https://github.com/astrophy/astrocrappy>

<sup>10</sup>[https://github.com/jselsing/XSGRB\\_reduction\\_scripts](https://github.com/jselsing/XSGRB_reduction_scripts)

<sup>11</sup>[https://github.com/finagle29/dbsp\\_drp](https://github.com/finagle29/dbsp_drp)

<sup>12</sup><https://mthamilton.ucolick.org/techdocs/instruments/kast/Tech%20Report%2066%20KAST%20Miller%20Stone.pdf>

<sup>13</sup><https://github.com/ishivvers/TheKastShiv>

<sup>14</sup>[https://www.swift.ac.uk/user\\_objects](https://www.swift.ac.uk/user_objects)

<sup>15</sup>The photon index is defined as the power-law index of the photon flux density ( $N(E) \propto E^{-\Gamma}$ ).

column density of  $2.7 \times 10^{20} \text{ cm}^{-2}$  [200]. The coadded count-rate limit translates to an unabsorbed flux of  $< 0.2 \times 10^{-13} \text{ erg cm}^{-2} \text{ s}^{-1}$  in the range of 0.3–10 keV and a luminosity of  $< 1.2 \times 10^{42} \text{ erg s}^{-1}$ . *Supplementary Material Table 4* shows a list of all limits.

Furthermore, we queried the NASA High Energy Astrophysics Science Archive Research Center (HEASARC<sup>16</sup>) to search for any X-ray and  $\gamma$ -ray transient preceding or accompanying SN 2021yfj. The source catalogues of the *Fermi*, *MAXI*, *NICER*, *NuSTAR*, *AGILE*, and *INTEGRAL* space missions returned no detection within  $10'$  from SN 2021yfj’s position between 1 August 2021 (32.7 days before the discovery of SN 2021yfj) and 4 February 2022 (131.8 days after the discovery of SN 2021yfj). Placing a detection limit is not possible for this multitude of facilities.

## Host-galaxy Observations

We retrieved science-ready coadded images from the *Galaxy Evolution Explorer* (*GALEX*) general release 6/7 [201], the DESI Legacy Imaging Surveys (LS; [116]) DR 10, and PS1. We measured the brightness of the host using LAMBDA (Lambda Adaptive Multi-Band Deblending Algorithm in R; [202]) and the methods described in Ref. [58]. The field was also observed by the VISTA Hemisphere Survey [203] in the near-IR. We measured the brightness with the aperture photometry tool presented in Ref. [127] using an aperture similar to the ones employed for the other images. The *GALEX*, LS, and PanSTARRS photometry was calibrated against tabulated zeropoints, and the VHS photometry against stars from the 2MASS Point Source Catalogue [204]. *Supplementary Material Table 5* summarises the measurements in the different bands.

The SN spectra also showed absorption lines from the ISM in the host and emission lines produced by the ionised gas in H II. *Supplementary Material Table 6* summarises the rest-frame equivalent widths of the absorption lines extracted from all early X-shooter spectra and the emission-line fluxes from X-shooter spectrum obtained at day 49.8. The flux measurements are not corrected for reddening.

## Comparison Objects

We compare the spectra and light curves of SN 2021yfj to those of other objects. Below, we list the relevant references for each object.

- SN 2006jc (Ibn) — bolometric light curve, not constructed; spectra, Ref. [12]
- SN 2010al (Ibn) — bolometric light curve, built with data from Ref. [205] using the programme *Superbol* [206]; spectra, Ref. [205]
- SN 2019hgp (Icn) — bolometric light curve, Ref. [13]; spectra, Ref. [13]
- SN 2020oi (Ic) — bolometric light curve, Ref. [207]
- SN 2021csp (Icn) — bolometric light curve, Ref. [14]; spectra, Ref. [14]

All spectra were retrieved from WISEREP.

---

<sup>16</sup><https://heasarc.gsfc.nasa.gov/cgi-bin/W3Browse/w3browse.pl>

**Supplementary Material Table 1:** Lines identified in the spectra shown in *Figure 1* and the *Extended Material Figure 3*.

Species	Lines (Å)
Ar III	3285.8, 3301.9, 3311.2, 3336.2, 3344.8, 3480.5, 3511.2, 3514.2
C III	4647.4, 4650.3, 4651.5, 7771.8
He I	3888.6, 5875.6, 7065.2, 10830
Mg II	2795.5 , 2802.7
S III	3324.0, 3324.8, 3367.2, 3369.5, 3370.4, 3387.1, 3497.3, 3499.2, 3632.0, 3661.9, 3710.4, 3717.7, 3747.9, 3750.7, 3794.6, 3837.7, 3838.3, 3860.6, 3928.6, 3983.7, 3985.9, 4091.2, 4253.5, 4284.9, 4354.5, 4361.5, 4364.7, 4418.8, 4677.6, 5160.1, 5219.3
S IV	3097.3, 3117.6, 3119.9, 3338.6, 3340.4, 3341.5
Si III	3096.8, 3185.1, 3241.6, 3486.8, 3590.5, 3796.1, 3806.5, 4552.6, 4567.8, 4574.8, 4716.7, 4813.3, 4819.7, 4828.95, 5739.73, 7461.9, 7466.3
Si IV	3149.6, 3165.7, 4088.9, 4116.1

**Notes:** These are the Ritz air wavelengths reported in the NIST atomic spectra database (details at <https://physics.nist.gov/PhysRefData/ASD/Html/lineshelp.html>). All wavelengths are rounded to one decimal place for convenience.

**Supplementary Material Table 2:** Log of photometric observations.

MJD	Phase (day)	Telescope/Instrument	Filter	Brightness (mag)
59466.102	1.5	<i>Swift</i> /UVOT	<i>w2</i>	20.23 ± 0.11
59466.951	2.2	<i>Swift</i> /UVOT	<i>w2</i>	20.59 ± 0.14
59467.683	2.9	<i>Swift</i> /UVOT	<i>w2</i>	20.62 ± 0.18
59468.744	3.8	<i>Swift</i> /UVOT	<i>w2</i>	20.56 ± 0.16
59469.546	4.5	<i>Swift</i> /UVOT	<i>w2</i>	20.51 ± 0.15
59470.830	5.6	<i>Swift</i> /UVOT	<i>w2</i>	20.41 ± 0.15

**Notes:** All measurements are reported in the AB system and are not corrected for reddening. The phase is reported in the rest-frame with respect to the time of the first detection (MJD=59464.414). Non-detections are reported at  $3\sigma$  confidence. A machine-readable table will be made available via the WISEREP archive and the journal webpage after the acceptance of the paper.



Supplementary Material Table 3: Log of spectroscopic observations.

MJD	Phase (day)	Telescope/Instrument	Dispenser	Slit width (′′)	Exposure time (s)	Wavelength range (Å)	Spectral resolution
59,465.57	1.0	Keck-I/LRIS	600/4000, 400/8500	1′′0	1,230	3,400 – 10,275	1,000/1,200
59,466.28	1.6	VLT/X-shooter	...	1′′0/0′′9/0′′9	3,000/2,900/2,880	3,000 – 24,800	5,400/8,900/5,600
59,467.28	2.5	VLT/X-shooter	...	1′′0/0′′9/0′′9	3,000/2,900/2,880	3,000 – 24,800	5,400/8,900/5,600
59,468.39	3.5	Lick/Kast	600/4310, 300/7500	2′′0, 2′′0	3,660/3,600	3,500 – 10,500	800
59,469.12	4.1	NOT/ALFOSC	Gr#4	1′′3	4,500	3,600 – 9,600	280
59,470.00	5.2	P200/DBSP	600/4000, 316/7500	1′′5	1,800	3,500 – 10,000	1,000/1,000
59,471.31	6.1	VLT/X-shooter	...	1′′0/0′′9/0′′9	3,000/2,900/2,880	3,000 – 24,800	5,400/8,900/5,600
59,473.16	7.7	NOT/ALFOSC	Gr#4	1′′0	4,500	3,600 – 9,600	360
59,477.05	11.1	NOT/ALFOSC	Gr#4	1′′3	4,500	3,600 – 9,600	280
59,487.21	20.0	VLT/X-shooter	...	1′′0/0′′9/0′′9	3,600/3,716/3,600	3,000 – 24,800	5,400/8,900/5,600
59,488.30	21.0	VLT/X-shooter	...	1′′0/0′′9/0′′9	3,000/2,900/2,880	3,000 – 24,800	5,400/8,900/5,600
59,491.52	23.8	Keck-I/LRIS	400/3400, 400/8500	1′′0	1,800	3,076 – 9,350	600/1,200
59,499.10	30.5	VLT/X-shooter	...	1′′0/0′′9/0′′9	4,400/4,400/3,840	3,000 – 24,800	5,400/8,900/5,600
59,521.13	49.8	VLT/X-shooter	...	1′′0/0′′9/0′′9	4,400/4,400/3,840	3,000 – 24,800	5,400/8,900/5,600
59,610.25	128.1	Keck-I/LRIS	600/4000, 400/8500	1′′0	3,600	3,400 – 10,275	1,000/1,200
59,615.27	132.5	Keck-I/LRIS	400/3400, 400/8500	1′′0	2,700	3,076 – 9,350	600/1,200

Notes: The modified Julian dates quote the beginning of each observation. The phase is reported for the mid-exposure time and in the rest frame with respect to the time of the first detection (MJD = 59,464.414). For the multi-arm instruments Kast, LRIS, and X-shooter, we report the exposure time and the spectral resolution of each arm. The wavelength ranges and the values of the spectral resolutions were taken from instrument manuals.

**Supplementary Material Table 4:** Log of X-ray observations.

MJD	Phase (day)	Count rate ( $10^{-3} \text{ s}^{-1}$ )	$F_X$ ( $10^{-13} \text{ erg s}^{-1} \text{ cm}^{-2}$ )	$L_X$ ( $10^{42} \text{ erg s}^{-1}$ )
<b>Unbinned data</b>				
59,466.10 ± 0.04	1.5	< 18.6	< 6.95	< 38.01
59,466.95 ± 0.04	2.2	< 6.0	< 2.24	< 12.24
59,467.68 ± 0.30	2.9	< 11.4	< 4.28	< 23.42
59,468.74 ± 0.10	3.8	< 5.7	< 2.14	< 11.68
59,469.55 ± 0.04	4.5	< 32.4	< 12.15	< 66.41
59,470.83 ± 0.01	5.6	< 7.4	< 2.78	< 15.21
59,473.49 ± 0.07	8.0	< 11.7	< 4.37	< 23.90
59,474.71 ± 0.04	9.0	< 4.7	< 1.75	< 9.59
59,476.84 ± 0.04	10.9	< 5.5	< 2.06	< 11.25
59,477.61 ± 0.07	11.6	< 4.7	< 1.76	< 9.61
59,483.02 ± 0.04	16.3	< 4.1	< 1.55	< 8.47
59,484.48 ± 0.44	17.6	< 3.9	< 1.46	< 7.97
59,486.90 ± 0.07	19.7	< 4.6	< 1.73	< 9.44
59,493.44 ± 0.23	25.5	< 11.6	< 4.34	< 23.72
59,496.06 ± 0.01	27.8	< 11.7	< 4.39	< 23.98
59,500.90 ± 0.01	32.0	< 9.4	< 3.51	< 19.18
59,581.30 ± 0.23	102.7	< 2.2	< 0.83	< 4.55
59,584.52 ± 0.01	105.5	< 17.7	< 6.65	< 36.33
59,633.42 ± 0.20	148.4	< 4.7	< 1.78	< 9.72
<b>Binned data</b>				
59,475.18 <sup>+158.45</sup> <sub>-9.12</sub>	9.5 <sup>+139.2</sup> <sub>-8.0</sub>	< 0.6	< 0.22	< 1.22

**Notes:** The modified Julian dates report the mid-exposure time. The phase is reported in the rest-frame with respect to the time of the first detection (MJD = 59,464.414). The time errors indicate the extent of the time bins. All limits are reported at  $3\sigma$  confidence. The measurements are corrected for MW absorption and are reported for the bandpass from 0.3 to 10 keV.

**Supplementary Material Table 5:** Photometry of the host galaxy.

Survey	Filter	Brightness (mag)	Survey	Filter	Brightness (mag)
<i>GALEX</i>	<i>FUV</i>	$23.04 \pm 0.19$	PS1	<i>g</i>	$21.58 \pm 0.11$
<i>GALEX</i>	<i>NUV</i>	$22.94 \pm 0.18$	PS1	<i>r</i>	$20.99 \pm 0.15$
LS	<i>g</i>	$21.45 \pm 0.02$	PS1	<i>i</i>	$20.73 \pm 0.08$
LS	<i>r</i>	$20.97 \pm 0.02$	VHS	<i>J</i>	$20.85 \pm 0.12$
LS	<i>i</i>	$20.68 \pm 0.03$	VHS	<i>H</i>	$20.46 \pm 0.09$
LS	<i>z</i>	$20.59 \pm 0.03$	VHS	<i>K<sub>s</sub></i>	$21.22 \pm 0.33$

**Notes:** All measurements are reported in the AB system and are not corrected for reddening.

**Supplementary Material Table 6:** Properties of the ISM in the host galaxy.

Transition	EW <sub>r</sub> (Å)	Flux ( $10^{-16}$ erg cm <sup>-2</sup> s <sup>-1</sup> )
<b>Absorption lines</b>		
Mg II $\lambda$ 2804	$1.02 \pm 0.06$	...
Mg I $\lambda$ 2852	$0.30 \pm 0.08$	...
<b>Emission lines</b>		
[O II] $\lambda$ 3926	...	$1.62 \pm 0.04$
[O II] $\lambda$ 3929	...	$2.36 \pm 0.04$
[Ne III] $\lambda$ 3869	...	$0.25 \pm 0.02$
H $\epsilon$	...	$0.12 \pm 0.02$
H $\delta$	...	$0.27 \pm 0.02$
H $\gamma$	...	$0.55 \pm 0.02$
[O III] $\lambda$ 4363 <sup>†</sup>	...	$0.04 \pm 0.03$
H $\beta$	...	$1.21 \pm 0.03$
[O III] $\lambda$ 4959	...	$0.84 \pm 0.04$
[O III] $\lambda$ 5007	...	$2.57 \pm 0.06$
[N II] $\lambda$ 6549	...	$0.23 \pm 0.02$
H $\alpha$	...	$4.87 \pm 0.05$
[N II] $\lambda$ 6584	...	$0.66 \pm 0.02$
[S II] $\lambda$ 6718	...	$0.92 \pm 0.03$
[S II] $\lambda$ 6732	...	$0.62 \pm 0.03$

**Notes:** We report rest-frame equivalent widths EW<sub>r</sub> for absorption lines and fluxes for emission lines. The emission lines are measured from the X-shooter spectrum at day 49.8 and are not corrected for reddening.

<sup>†</sup> Measurement has a significance of  $< 3\sigma$ .

**Supplementary Material Table 7:** The bolometric light curve and blackbody properties.

Phase (day)	$\log L_{\text{bol}}$ ( $\text{erg s}^{-1}$ ) (1,800–7,850 Å)	$\log L_{\text{bol}}$ ( $\text{erg s}^{-1}$ ) (+FUV +IR)	$T_{\text{BB}}$ (K)	$\log R_{\text{BB}}$ (cm)	Bolometric correction?
0	$43.38 \pm 0.09$	$43.60 \pm 0.08$	...	...	yes
0.28	$43.42 \pm 0.07$	$43.62 \pm 0.07$	...	...	yes
0.78	$43.45 \pm 0.06$	$43.64 \pm 0.06$	...	...	yes
1.28	$43.49 \pm 0.05$	$43.67 \pm 0.05$	...	...	yes
1.78	$43.52 \pm 0.04$	$43.69 \pm 0.05$	$15,522 \pm 998$	$15.00 \pm 0.04$	no
2.28	$43.52 \pm 0.04$	$43.68 \pm 0.05$	$15,351 \pm 936$	$15.00 \pm 0.04$	no

**Notes:** The phase is reported in the rest frame with respect to the time of the first detection (MJD = 59,464.414). The last column indicates whether a bolometric correction was applied to determine the pseudobolometric luminosity in the wavelength interval 1,800–7,850 Å. Including the missing FUV and IR flux required a bolometric correction for all data (see the *Methods Section Bolometric Light Curve* for details). The blackbody properties are only reported where UV and optical photometry are available and where the spectrum is adequately described by a blackbody. A machine-readable table will be made available via the WISeREP archive and the journal webpage after the acceptance of the paper.

**Supplementary Material Table 8:** Light-curve fits with Redback: models, priors and marginalised posteriors.

Parameter	Prior	Magnetar	Nickel
<b>General</b>			
ejecta mass $M_{\text{ej}}$ ( $M_{\odot}$ )	$\log \mathcal{U}(0.01, 10)$	$0.3^{+0.3}_{-0.1}$	$1.7 \pm 0.1$
explosion date $t_{\text{exp}}$ (day, observer frame)	$\mathcal{U}(-10, 0)$	$-4.5^{+1.0}_{-0.3}$	$-8.3 \pm 0.5$
“ $\gamma$ -ray” opacity $\kappa_{\gamma}$ ( $\text{cm}^2 \text{g}^{-1}$ )	$\log \mathcal{U}(10^{-4}, 10^4)$	$0.09^{+0.06}_{-0.03}$	0.034 (fixed)
optical opacity $\kappa$ ( $\text{cm}^2 \text{g}^{-1}$ )	$\mathcal{U}(0.01, 0.5)$	$0.01 \pm 0.01$	0.07 (fixed)
photospheric plateau temperature $T$ (K)	$\mathcal{U}(5000, 15,000)$	$14,600^{+300}_{-400}$	$14,200 \pm 300$
white-noise parameter $\sigma$	$\mathcal{U}(10^{-3}, 2)$	0.01	0.01
V-band absorption $A_V$ (mag)	$\mathcal{U}(0, 1)$	$0.08^{+0.08}_{-0.05}$	$0.01 \pm 0.01$
<b>Magnetar model</b>			
ejecta nickel mass fraction $f_{\text{Ni}}$	$\log \mathcal{U}(10^{-3}, 1)$	$0.05^{+0.32}_{-0.05}$	...
initial spin-down luminosity $L_0$ ( $10^{44} \text{erg s}^{-1}$ )	$\log \mathcal{U}(10^{-4}, 10^6)$	$0.9^{+2.1}_{-0.2}$	...
braking index $n$	$\mathcal{U}(1.5, 10)$	$7.9^{+1.4}_{-1.8}$	...
spin-down time $\tau_{\text{sd}}$ (s)	$\log \mathcal{U}(10, 10^8)$	$1.3^{+0.8}_{-1.0} \times 10^6$	...
supernova explosion energy $E_{\text{SN}}$ ( $10^{50} \text{erg}$ )	$\mathcal{U}(1, 50)$	$1.9^{+1.0}_{-0.6}$	...
<b><math>^{56}\text{Ni}</math> model</b>			
ejecta nickel mass fraction $f_{\text{Ni}}$	$\log \mathcal{U}(10^{-3}, 1)$	...	$0.97 \pm 0.01$
scaling velocity $v_{\text{scale}}$ ( $\text{km s}^{-1}$ )	$\mathcal{U}(1000, 15,000)$	...	$14,300^{+400}_{-600}$
<b>Fit quality</b>			
log Bayesian evidence ( $\log Z$ )		547	518
number of free parameters		12	7

**Notes:** We used uniform ( $\mathcal{U}$ ) and log-uniform ( $\log \mathcal{U}$ ) priors. The uncertainties of the marginalised posteriors are quoted at  $1\sigma$  confidence. The explosion date is measured with respect to the time of the first detection. All marginalised posteriors are reported in linear units. The Bayesian evidence is reported in log units. The opacities of the nickel model were taken from Refs. [208, 209].

**Supplementary Material Table 9:** Light curve fit with CHIPS.

Parameter	Value
ejecta mass $M_{\text{ej}}$ ( $M_{\odot}$ )	5
CSM mass $M_{\text{CSM}}$ ( $M_{\odot}$ )	$> 1$
explosion energy $E_{\text{ej}}$ (erg)	$1.6 \times 10^{51}$
power-law index of the inner CSM $n_{\text{in}}$	1.1
radius at transition $r_{\text{CSM}}$ (cm)	$5 \times 10^{15}$
density at transition $\hat{\rho}_{\text{CSM}}$ ( $\text{g cm}^{-3}$ )	$3 \times 10^{-15}$

## References

- [1] Burbidge, E. M., Burbidge, G. R., Fowler, W. A. & Hoyle, F. Synthesis of the Elements in Stars. *Reviews of Modern Physics* **29**, 547–650 (1957).
- [2] Kippenhahn, R., Weigert, A. & Weiss, A. *Stellar Structure and Evolution* (Springer Berlin, Heidelberg, 2013).
- [3] Arcones, A. & Thielemann, F.-K. Origin of the elements. *Astron. Astrophys. Rev.* **31**, 1 (2023).
- [4] Woosley, S. E. & Weaver, T. A. The Evolution and Explosion of Massive Stars. II. Explosive Hydrodynamics and Nucleosynthesis. *Astrophys. J. Suppl. Ser.* **101**, 181 (1995).
- [5] Woosley, S. E., Heger, A. & Weaver, T. A. The evolution and explosion of massive stars. *Reviews of Modern Physics* **74**, 1015–1071 (2002).
- [6] Heger, A., Fryer, C. L., Woosley, S. E., Langer, N. & Hartmann, D. H. How Massive Single Stars End Their Life. *Astrophys. J.* **591**, 288–300 (2003).
- [7] Woosley, S. E. & Janka, T. The physics of core-collapse supernovae. *Nature Physics* **1**, 147–154 (2005).
- [8] Müller, B. The Status of Multi-Dimensional Core-Collapse Supernova Models. *Publ. Astron. Soc. Aust.* **33**, e048 (2016).
- [9] Woosley, S. E. Pulsational Pair-instability Supernovae. *Astrophys. J.* **836**, 244 (2017).
- [10] Crowther, P. A. Physical Properties of Wolf-Rayet Stars. *Annu. Rev. Astron. Astrophys.* **45**, 177–219 (2007).
- [11] Matheson, T., Filippenko, A. V., Ho, L. C., Barth, A. J. & Leonard, D. C. Detailed Analysis of Early to Late-Time Spectra of Supernova 1993J. *Astron. J.* **120**, 1499–1515 (2000).
- [12] Pastorello, A. *et al.* A giant outburst two years before the core-collapse of a massive star. *Nature* **447**, 829–832 (2007).
- [13] Gal-Yam, A. *et al.* A WC/WO star exploding within an expanding carbon-oxygen-neon nebula. *Nature* **601**, 201–204 (2022).
- [14] Perley, D. A. *et al.* The Type Icn SN 2021csp: Implications for the Origins of the Fastest Supernovae and the Fates of Wolf-Rayet Stars. *Astrophys. J.* **927**, 180 (2022).
- [15] Maeda, K. & Moriya, T. J. Properties of Type Ibn Supernovae: Implications for the Progenitor Evolution and the Origin of a Population of Rapid Transients. *Astrophys. J.* **927**, 25 (2022).
- [16] Bellm, E. C. *et al.* The Zwicky Transient Facility: System Overview, Performance, and First Results. *Publ. Astron. Soc. Pac.* **131**, 018002 (2019).
- [17] Graham, M. J. *et al.* The Zwicky Transient Facility: Science Objectives. *Publ. Astron. Soc. Pac.* **131**, 078001 (2019).
- [18] Muñoz-Arancibia, A. *et al.* ALerCE/ZTF Transient Discovery Report for 2021-09-07. *Transient Name Server Discovery Report* **2021-3075**, 1–3075 (2021).
- [19] Bruch, R. J. *et al.* The Prevalence and Influence of Circumstellar Material around Hydrogen-rich Supernova Progenitors. *Astrophys. J.* **952**, 119 (2023).
- [20] Pastorello, A. *et al.* Massive stars exploding in a He-rich circumstellar medium - I. Type Ibn (SN 2006jc-like) events. *Mon. Not. R. Astron. Soc.* **389**, 113–130 (2008).

- [21] Bruch, R. J. *et al.* A Large Fraction of Hydrogen-rich Supernova Progenitors Experience Elevated Mass Loss Shortly Prior to Explosion. *Astrophys. J.* **912**, 46 (2021).
- [22] Jacobson-Galán, W. V. *et al.* Final Moments. II. Observational Properties and Physical Modeling of Circumstellar-material-interacting Type II Supernovae. *Astrophys. J.* **970**, 189 (2024).
- [23] Planck Collaboration *et al.* Planck 2018 results. VI. Cosmological parameters. *Astron. Astrophys.* **641**, A6 (2020).
- [24] Liu, Y.-Q., Modjaz, M. & Bianco, F. B. Analyzing the Largest Spectroscopic Data Set of Hydrogen-poor Super-luminous Supernovae. *Astrophys. J.* **845**, 85 (2017).
- [25] Dessart, L., Hillier, D. J. & Kuncarayakti, H. Helium stars exploding in circumstellar material and the origin of Type Ibn supernovae. *Astron. Astrophys.* **658**, A130 (2022).
- [26] Filippenko, A. V. Optical Spectra of Supernovae. *Annu. Rev. Astron. Astrophys.* **35**, 309–355 (1997).
- [27] Gal-Yam, A. in *Observational and Physical Classification of Supernovae* (eds Alsabti, A. W. & Murdin, P.) *Handbook of Supernovae* 195 (Springer Cham, 2017).
- [28] Gal-Yam, A., Yaron, O. & Schulze, S. Introducing a new supernova classification type: SN Ien. *Transient Name Server AstroNote* **239** (2024).
- [29] Takei, Y., Tsuna, D., Kuriyama, N., Ko, T. & Shigeyama, T. CHIPS: Complete History of Interaction-powered Supernovae. *Astrophys. J.* **929**, 177 (2022).
- [30] Takei, Y., Tsuna, D., Ko, T. & Shigeyama, T. Simulating Hydrogen-poor Interaction-powered Supernovae with CHIPS. *Astrophys. J.* **961**, 67 (2024).
- [31] Elmhamdi, A. *et al.* Photometry and spectroscopy of the Type IIP SN 1999em from outburst to dust formation. *Mon. Not. R. Astron. Soc.* **338**, 939–956 (2003).
- [32] Dessart, L. & Hillier, D. J. Quantitative spectroscopy of photospheric-phase type II supernovae. *Astron. Astrophys.* **437**, 667–685 (2005).
- [33] Dessart, L. & Hillier, D. J. Non-LTE time-dependent spectroscopic modelling of Type II-plateau supernovae from the photospheric to the nebular phase: case study for 15 and 25  $M_{\odot}$  progenitor stars. *Mon. Not. R. Astron. Soc.* **410**, 1739–1760 (2011).
- [34] Hillier, D. J. & Dessart, L. Photometric and spectroscopic diversity of Type II supernovae. *Astron. Astrophys.* **631**, A8 (2019).
- [35] Dessart, L., Yoon, S.-C., Aguilera-Dena, D. R. & Langer, N. Supernovae Ib and Ic from the explosion of helium stars. *Astron. Astrophys.* **642**, A106 (2020).
- [36] Fowler, W. A. & Hoyle, F. Neutrino Processes and Pair Formation in Massive Stars and Supernovae. *Astrophys. J. Suppl. Ser.* **9**, 201 (1964).
- [37] Barkat, Z., Rakavy, G. & Sack, N. Dynamics of Supernova Explosion Resulting from Pair Formation. *Phys. Rev. Lett.* **18**, 379–381 (1967).
- [38] Rakavy, G., Shaviv, G. & Zinamon, Z. Carbon and Oxygen Burning Stars and Pre-Supernova Models. *Astrophys. J.* **150**, 131 (1967).
- [39] Leung, S.-C., Nomoto, K. & Blinnikov, S. Pulsational Pair-instability Supernovae. I. Pre-collapse Evolution and Pulsational Mass Ejection. *Astrophys. J.* **887**, 72 (2019).
- [40] Marchant, P. *et al.* Pulsational Pair-instability Supernovae in Very Close Binaries. *Astrophys. J.*

882, 36 (2019).

- [41] Gal-Yam, A. *et al.* A Wolf-Rayet-like progenitor of SN 2013cu from spectral observations of a stellar wind. *Nature* **509**, 471–474 (2014).
- [42] Groh, J. H. Early-time spectra of supernovae and their precursor winds. The luminous blue variable/yellow hypergiant progenitor of SN 2013cu. *Astron. Astrophys.* **572**, L11 (2014).
- [43] Yaron, O. *et al.* Confined dense circumstellar material surrounding a regular type II supernova. *Nature Physics* **13**, 510–517 (2017).
- [44] Fremling, C. *et al.* The Zwicky Transient Facility Bright Transient Survey. I. Spectroscopic Classification and the Redshift Completeness of Local Galaxy Catalogs. *Astrophys. J.* **895**, 32 (2020).
- [45] Perley, D. A. *et al.* The Zwicky Transient Facility Bright Transient Survey. II. A Public Statistical Sample for Exploring Supernova Demographics. *Astrophys. J.* **904**, 35 (2020).
- [46] Li, W. *et al.* Nearby supernova rates from the Lick Observatory Supernova Search - II. The observed luminosity functions and fractions of supernovae in a complete sample. *Mon. Not. R. Astron. Soc.* **412**, 1441–1472 (2011).
- [47] LSST Science Collaboration *et al.* LSST Science Book, Version 2.0. *arXiv e-prints* arXiv:0912.0201 (2009).
- [48] Tonry, J. L. An Early Warning System for Asteroid Impact. *Publ. Astron. Soc. Pac.* **123**, 58 (2011).
- [49] Smith, K. W. *et al.* Design and Operation of the ATLAS Transient Science Server. *Publ. Astron. Soc. Pac.* **132**, 085002 (2020).
- [50] Jones, D. O. *et al.* The Young Supernova Experiment: Survey Goals, Overview, and Operations. *Astrophys. J.* **908**, 143 (2021).
- [51] Steeghs, D. *et al.* The Gravitational-wave Optical Transient Observer (GOTO): prototype performance and prospects for transient science. *Mon. Not. R. Astron. Soc.* **511**, 2405–2422 (2022).
- [52] Ofek, E. O. *et al.* The Large Array Survey Telescope-System Overview and Performances. *Publ. Astron. Soc. Pac.* **135**, 065001 (2023).
- [53] Groot, P. J. *et al.* The BlackGEM telescope array I: Overview. *arXiv e-prints* arXiv:2405.18923 (2024).
- [54] Liu, Y.-Q., Modjaz, M., Bianco, F. B. & Graur, O. Analyzing the Largest Spectroscopic Data Set of Stripped Supernovae to Improve Their Identifications and Constrain Their Progenitors. *Astrophys. J.* **827**, 90 (2016).
- [55] Sarin, N. *et al.* REDBACK: a Bayesian inference software package for electromagnetic transients. *Mon. Not. R. Astron. Soc.* **531**, 1203–1227 (2024).
- [56] Soumagnac, M. T. *et al.* Early Ultraviolet Observations of Type II<sub>n</sub> Supernovae Constrain the Asphericity of Their Circumstellar Material. *Astrophys. J.* **899**, 51 (2020).
- [57] Elbaz, D. *et al.* The reversal of the star formation-density relation in the distant universe. *Astron. Astrophys.* **468**, 33–48 (2007).
- [58] Schulze, S. *et al.* The Palomar Transient Factory Core-collapse Supernova Host-galaxy Sample. I. Host-galaxy Distribution Functions and Environment Dependence of Core-collapse Supernovae. *Astrophys. J. Suppl. Ser.* **255**, 29 (2021).



- [59] Johnson, B. D., Leja, J., Conroy, C. & Speagle, J. S. Stellar Population Inference with Prospector. *Astrophys. J. Suppl. Ser.* **254**, 22 (2021).
- [60] Masci, F. J. *et al.* The Zwicky Transient Facility: Data Processing, Products, and Archive. *Publ. Astron. Soc. Pac.* **131**, 018003 (2019).
- [61] Patterson, M. T. *et al.* The Zwicky Transient Facility Alert Distribution System. *Publ. Astron. Soc. Pac.* **131**, 018001 (2019).
- [62] Zackay, B., Ofek, E. O. & Gal-Yam, A. Proper Image Subtraction—Optimal Transient Detection, Photometry, and Hypothesis Testing. *Astrophys. J.* **830**, 27 (2016).
- [63] Gal-Yam, A. The Most Luminous Supernovae. *Annu. Rev. Astron. Astrophys.* **57**, 305–333 (2019).
- [64] van der Walt, S., Crellin-Quick, A. & Bloom, J. SkyPortal: An Astronomical Data Platform. *The Journal of Open Source Software* **4**, 1247 (2019).
- [65] Coughlin, M. W. *et al.* A Data Science Platform to Enable Time-domain Astronomy. *Astrophys. J. Suppl. Ser.* **267**, 31 (2023).
- [66] Gal-Yam, A. *et al.* Real-time Detection and Rapid Multiwavelength Follow-up Observations of a Highly Subluminous Type II-P Supernova from the Palomar Transient Factory Survey. *Astrophys. J.* **736**, 159 (2011).
- [67] Förster, F. *et al.* The Automatic Learning for the Rapid Classification of Events (ALeRCE) Alert Broker. *Astron. J.* **161**, 242 (2021).
- [68] Huber, M. *et al.* The Pan-STARRS Survey for Transients (PSST) - first announcement and public release. *The Astronomer's Telegram* **7153**, 1 (2015).
- [69] Gal-Yam, A. *et al.* The spectroscopic classification of SN 2021yfj. *Transient Name Server Classification Report* **2024-17883** (2024).
- [70] Gal-Yam, A. *et al.* The spectroscopic classification of SN 2021yfj. *Transient Name Server AstroNote* **240** (2024).
- [71] Strotjohann, N. L. *et al.* Bright, Months-long Stellar Outbursts Announce the Explosion of Interaction-powered Supernovae. *Astrophys. J.* **907**, 99 (2021).
- [72] Hogg, D. W., Baldry, I. K., Blanton, M. R. & Eisenstein, D. J. The K correction. *arXiv e-prints astro-ph/0210394* (2002).
- [73] Miller, A. A. *et al.* ZTF Early Observations of Type Ia Supernovae. II. First Light, the Initial Rise, and Time to Reach Maximum Brightness. *Astrophys. J.* **902**, 47 (2020).
- [74] Maguire, K. in *Type Ia Supernovae* (eds Alsabti, A. W. & Murdin, P.) *Handbook of Supernovae* 293 (Springer Cham, 2017).
- [75] Arcavi, I. in *Hydrogen-Rich Core-Collapse Supernovae* (eds Alsabti, A. W. & Murdin, P.) *Handbook of Supernovae* 239 (Springer Cham, 2017).
- [76] Gezari, S. Tidal Disruption Events. *Annu. Rev. Astron. Astrophys.* **59**, 21–58 (2021).
- [77] Bond, H. E. *et al.* The 2008 Luminous Optical Transient in the Nearby Galaxy NGC 300. *Astrophys. J. Lett.* **695**, L154–L158 (2009).
- [78] Ho, A. Y. Q. *et al.* A Search for Extragalactic Fast Blue Optical Transients in ZTF and the Rate of AT2018scow-like Transients. *Astrophys. J.* **949**, 120 (2023).

- [79] De, K. *et al.* The Zwicky Transient Facility Census of the Local Universe. I. Systematic Search for Calcium-rich Gap Transients Reveals Three Related Spectroscopic Subclasses. *Astrophys. J.* **905**, 58 (2020).
- [80] Pastorello, A. *et al.* Luminous red novae: Stellar mergers or giant eruptions? *Astron. Astrophys.* **630**, A75 (2019).
- [81] Liu, F. T., Ting, K. M. & Zhou, Z.-H. *Isolation forest*, 413–422 (IEEE, 2008).
- [82] Pedregosa, F. *et al.* Scikit-learn: Machine learning in Python. *Journal of Machine Learning Research* **12**, 2825–2830 (2011).
- [83] Nicholl, M. *et al.* SN 2015bn: A Detailed Multi-wavelength View of a Nearby Superluminous Supernova. *Astrophys. J.* **826**, 39 (2016).
- [84] Schulze, S. *et al.* 1100 days in the life of the supernova 2018ibb. The best pair-instability supernova candidate, to date. *Astron. Astrophys.* **683**, A223 (2024).
- [85] Kool, E. C. *et al.* SN 2020bqj: A Type Ibn supernova with a long-lasting peak plateau. *Astron. Astrophys.* **652**, A136 (2021).
- [86] Ofek, E. O. *et al.* SN 2010jl: Optical to Hard X-Ray Observations Reveal an Explosion Embedded in a Ten Solar Mass Cocoon. *Astrophys. J.* **781**, 42 (2014).
- [87] Arnett, W. D. Type I supernovae. I - Analytic solutions for the early part of the light curve. *Astrophys. J.* **253**, 785–797 (1982).
- [88] Kasen, D. & Bildsten, L. Supernova Light Curves Powered by Young Magnetars. *Astrophys. J.* **717**, 245–249 (2010).
- [89] Omand, C. M. B. & Sarin, N. A generalized semi-analytic model for magnetar-driven supernovae. *Mon. Not. R. Astron. Soc.* **527**, 6455–6472 (2024).
- [90] Jeffery, D. J. Radioactive Decay Energy Deposition in Supernovae and the Exponential/Quasi-Exponential Behavior of Late-Time Supernova Light Curves. *arXiv e-prints* astro-ph/9907015 (1999).
- [91] Williams, M. J. nessai: Nested sampling with artificial intelligence (2021). URL <https://doi.org/10.5281/zenodo.4550693>.
- [92] Williams, M. J., Veitch, J. & Messenger, C. Nested sampling with normalizing flows for gravitational-wave inference. *Phys. Rev. D* **103**, 103006 (2021).
- [93] Williams, M. J., Veitch, J. & Messenger, C. Importance nested sampling with normalising flows (2023).
- [94] Ashton, G. *et al.* BILBY: A User-friendly Bayesian Inference Library for Gravitational-wave Astronomy. *Astrophys. J. Suppl. Ser.* **241**, 27 (2019).
- [95] Romero-Shaw, I. M. *et al.* Bayesian inference for compact binary coalescences with BILBY: validation and application to the first LIGO-Virgo gravitational-wave transient catalogue. *Mon. Not. R. Astron. Soc.* **499**, 3295–3319 (2020).
- [96] Matzner, C. D. & McKee, C. F. The Expulsion of Stellar Envelopes in Core-Collapse Supernovae. *Astrophys. J.* **510**, 379–403 (1999).
- [97] Moriya, T. J. *et al.* An analytic bolometric light curve model of interaction-powered supernovae and its application to Type IIn supernovae. *Mon. Not. R. Astron. Soc.* **435**, 1520–1535 (2013).

- [98] Owocki, S. P., Hirai, R., Podsiadlowski, P. & Schneider, F. R. N. Hydrodynamical simulations and similarity relations for eruptive mass-loss from massive stars. *Mon. Not. R. Astron. Soc.* **485**, 988–1000 (2019).
- [99] Tsuna, D., Takei, Y., Kuriyama, N. & Shigeyama, T. An analytical density profile of dense circumstellar medium in Type II supernovae. *Publ. Astron. Soc. Jpn* **73**, 1128–1136 (2021).
- [100] Tsuna, D. & Takei, Y. Detached and continuous circumstellar matter in Type Ibc supernovae from mass eruption. *Publ. Astron. Soc. Jpn* **75**, L19–L25 (2023).
- [101] Magee, N. H. *et al.* Adelman, S. J. & Wiese, W. L. (eds) *Atomic Structure Calculations and New LOS Alamos Astrophysical Opacities*. (eds Adelman, S. J. & Wiese, W. L.) *Astrophysical Applications of Powerful New Databases*, Vol. 78 of *Astronomical Society of the Pacific Conference Series*, 51 (1995).
- [102] Chevalier, R. A. & Fransson, C. Pulsar Nebulae in Supernovae. *Astrophys. J.* **395**, 540 (1992).
- [103] Chevalier, R. A. & Fransson, C. Emission from Circumstellar Interaction in Normal Type II Supernovae. *Astrophys. J.* **420**, 268 (1994).
- [104] Chandra, P. *et al.* Radio and X-Ray Observations of SN 2006jd: Another Strongly Interacting Type II In Supernova. *Astrophys. J.* **755**, 110 (2012).
- [105] Dwarkadas, V. V. & Gruszko, J. What are published X-ray light curves telling us about young supernova expansion? *Mon. Not. R. Astron. Soc.* **419**, 1515–1524 (2012).
- [106] Chandra, P., Chevalier, R. A., Chugai, N., Fransson, C. & Soderberg, A. M. X-Ray and Radio Emission from Type II In Supernova SN 2010jl. *Astrophys. J.* **810**, 32 (2015).
- [107] Gal-Yam, A. A Simple Analysis of Type I Superluminous Supernova Peak Spectra: Composition, Expansion Velocities, and Dynamics. *Astrophys. J.* **882**, 102 (2019).
- [108] Kramida, A., Yu. Ralchenko, Reader, J. & and NIST ASD Team. NIST Atomic Spectra Database (ver. 5.5.6), [Online]. Available: <https://physics.nist.gov/asd> [2018, April 6]. National Institute of Standards and Technology, Gaithersburg, MD. (2018).
- [109] Hosseinzadeh, G. *et al.* Type Ibn Supernovae Show Photometric Homogeneity and Spectral Diversity at Maximum Light. *Astrophys. J.* **836**, 158 (2017).
- [110] Asplund, M., Grevesse, N., Sauval, A. J. & Scott, P. The Chemical Composition of the Sun. *Annu. Rev. Astron. Astrophys.* **47**, 481–522 (2009).
- [111] Irani, I. *et al.* The Early Ultraviolet Light Curves of Type II Supernovae and the Radii of Their Progenitor Stars. *Astrophys. J.* **970**, 96 (2024).
- [112] Anupama, G. C. *et al.* Optical photometry and spectroscopy of the Type Ibn supernova SN 2006jc until the onset of dust formation. *Mon. Not. R. Astron. Soc.* **392**, 894–903 (2009).
- [113] Foley, R. J. *et al.* SN 2006jc: A Wolf-Rayet Star Exploding in a Dense He-rich Circumstellar Medium. *Astrophys. J. Lett.* **657**, L105–L108 (2007).
- [114] Kuncarayakti, H. *et al.* Late-time H/He-poor Circumstellar Interaction in the Type Ic Supernova SN 2021ocs: An Exposed Oxygen-Magnesium Layer and Extreme Stripping of the Progenitor. *Astrophys. J. Lett.* **941**, L32 (2022).
- [115] Dessart, L., Hillier, D. J., Sukhbold, T., Woosley, S. E. & Janka, H. T. Nebular phase properties of supernova Ibc from He-star explosions. *Astron. Astrophys.* **656**, A61 (2021).
- [116] Dey, A. *et al.* Overview of the DESI Legacy Imaging Surveys. *Astron. J.* **157**, 168 (2019).

- [117] Bertin, E. Ballester, P., Egret, D. & Lorente, N. P. F. (eds) *Displaying Digital Deep Sky Images*. (eds Ballester, P., Egret, D. & Lorente, N. P. F.) *Astronomical Data Analysis Software and Systems XXI*, Vol. 461 of *Astronomical Society of the Pacific Conference Series*, 263 (2012).
- [118] Conroy, C., Gunn, J. E. & White, M. The Propagation of Uncertainties in Stellar Population Synthesis Modeling. I. The Relevance of Uncertain Aspects of Stellar Evolution and the Initial Mass Function to the Derived Physical Properties of Galaxies. *Astrophys. J.* **699**, 486–506 (2009).
- [119] Foreman-Mackey, D., Sick, J. & Johnson, B. Python-Fsps: Python Bindings To Fsps (V0.1.1) (2014).
- [120] Byler, N., Dalcanton, J. J., Conroy, C. & Johnson, B. D. Nebular Continuum and Line Emission in Stellar Population Synthesis Models. *Astrophys. J.* **840**, 44 (2017).
- [121] Speagle, J. S. DYNESTY: a dynamic nested sampling package for estimating Bayesian posteriors and evidences. *Mon. Not. R. Astron. Soc.* **493**, 3132–3158 (2020).
- [122] Chabrier, G. Galactic Stellar and Substellar Initial Mass Function. *Publ. Astron. Soc. Pac.* **115**, 763 (2003).
- [123] Calzetti, D. *et al.* The Dust Content and Opacity of Actively Star-forming Galaxies. *Astrophys. J.* **533**, 682–695 (2000).
- [124] Law, N. M. *et al.* The Palomar Transient Factory: System Overview, Performance, and First Results. *Publ. Astron. Soc. Pac.* **121**, 1395 (2009).
- [125] Rau, A. *et al.* Exploring the Optical Transient Sky with the Palomar Transient Factory. *Publ. Astron. Soc. Pac.* **121**, 1334 (2009).
- [126] Kulkarni, S. R. The intermediate Palomar Transient Factory (iPTF) begins. *The Astronomer’s Telegram* **4807**, 1 (2013).
- [127] Schulze, S. *et al.* Cosmic evolution and metal aversion in superluminous supernova host galaxies. *Mon. Not. R. Astron. Soc.* **473**, 1258–1285 (2018).
- [128] Pellegrino, C. *et al.* The Diverse Properties of Type Icn Supernovae Point to Multiple Progenitor Channels. *Astrophys. J.* **938**, 73 (2022).
- [129] Osterbrock, D. E. & Ferland, G. J. *Astrophysics of gaseous nebulae and active galactic nuclei* (University Science Books, 2006).
- [130] Kennicutt, J., Robert C. Star Formation in Galaxies Along the Hubble Sequence. *Annu. Rev. Astron. Astrophys.* **36**, 189–232 (1998).
- [131] Madau, P. & Dickinson, M. Cosmic Star-Formation History. *Annu. Rev. Astron. Astrophys.* **52**, 415–486 (2014).
- [132] Pettini, M. & Pagel, B. E. J. [OIII]/[NII] as an abundance indicator at high redshift. *Mon. Not. R. Astron. Soc.* **348**, L59–L63 (2004).
- [133] Curti, M. *et al.* New fully empirical calibrations of strong-line metallicity indicators in star-forming galaxies. *Mon. Not. R. Astron. Soc.* **465**, 1384–1400 (2017).
- [134] Andrews, B. H. & Martini, P. The Mass-Metallicity Relation with the Direct Method on Stacked Spectra of SDSS Galaxies. *Astrophys. J.* **765**, 140 (2013).
- [135] Vink, J. S. Theory and Diagnostics of Hot Star Mass Loss. *Annu. Rev. Astron. Astrophys.* **60**, 203–246 (2022).

- [136] Smith, N. Mass Loss: Its Effect on the Evolution and Fate of High-Mass Stars. *Annu. Rev. Astron. Astrophys.* **52**, 487–528 (2014).
- [137] Humphreys, R. M. & Davidson, K. The Luminous Blue Variables: Astrophysical Geysers. *Publ. Astron. Soc. Pac.* **106**, 1025 (1994).
- [138] Podsiadlowski, P., Joss, P. C. & Hsu, J. J. L. Presupernova Evolution in Massive Interacting Binaries. *Astrophys. J.* **391**, 246 (1992).
- [139] Marchant, P. & Bodensteiner, J. The Evolution of Massive Binary Stars. *arXiv e-prints arXiv:2311.01865* (2023).
- [140] Heger, A. & Woosley, S. E. The Nucleosynthetic Signature of Population III. *Astrophys. J.* **567**, 532–543 (2002).
- [141] Umeda, H. & Nomoto, K. Nucleosynthesis of Zinc and Iron Peak Elements in Population III Type II Supernovae: Comparison with Abundances of Very Metal Poor Halo Stars. *Astrophys. J.* **565**, 385–404 (2002).
- [142] Kasen, D., Woosley, S. E. & Heger, A. Pair Instability Supernovae: Light Curves, Spectra, and Shock Breakout. *Astrophys. J.* **734**, 102 (2011).
- [143] Kozyreva, A. *et al.* Fast evolving pair-instability supernova models: evolution, explosion, light curves. *Mon. Not. R. Astron. Soc.* **464**, 2854–2865 (2017).
- [144] Gilmer, M. S., Kozyreva, A., Hirschi, R., Fröhlich, C. & Yusof, N. Pair-instability Supernova Simulations: Progenitor Evolution, Explosion, and Light Curves. *Astrophys. J.* **846**, 100 (2017).
- [145] Woosley, S. E., Blinnikov, S. & Heger, A. Pulsational pair instability as an explanation for the most luminous supernovae. *Nature* **450**, 390–392 (2007).
- [146] Yoshida, T., Umeda, H., Maeda, K. & Ishii, T. Mass ejection by pulsational pair instability in very massive stars and implications for luminous supernovae. *Mon. Not. R. Astron. Soc.* **457**, 351–361 (2016).
- [147] Farmer, R., Renzo, M., de Mink, S. E., Fishbach, M. & Justham, S. Constraints from Gravitational-wave Detections of Binary Black Hole Mergers on the  $^{12}\text{C}(\alpha, \gamma)^{16}\text{O}$  Rate. *Astrophys. J. Lett.* **902**, L36 (2020).
- [148] Woosley, S. E. & Heger, A. The Pair-instability Mass Gap for Black Holes. *Astrophys. J. Lett.* **912**, L31 (2021).
- [149] Farag, E., Renzo, M., Farmer, R., Chidester, M. T. & Timmes, F. X. Resolving the Peak of the Black Hole Mass Spectrum. *Astrophys. J.* **937**, 112 (2022).
- [150] Chen, K.-J., Woosley, S., Heger, A., Almgren, A. & Whalen, D. J. Two-dimensional Simulations of Pulsational Pair-instability Supernovae. *Astrophys. J.* **792**, 28 (2014).
- [151] Chen, K.-J., Whalen, D. J., Woosley, S. E. & Zhang, W. Multidimensional Radiation Hydrodynamics Simulations of Pulsational Pair-instability Supernovae. *Astrophys. J.* **955**, 39 (2023).
- [152] Woosley, S. E. & Heger, A. The Remarkable Deaths of 9-11 Solar Mass Stars. *Astrophys. J.* **810**, 34 (2015).
- [153] Woosley, S. E. The Evolution of Massive Helium Stars, Including Mass Loss. *Astrophys. J.* **878**, 49 (2019).
- [154] Woosley, S. E. & Bloom, J. S. The Supernova Gamma-Ray Burst Connection. *Annu. Rev. Astron. Astrophys.* **44**, 507–556 (2006).

- [155] Hjorth, J. & Bloom, J. S. in *The Gamma-Ray Burst - Supernova Connection* (eds Kouveliotou, C., Wijers, R. A. M. J. & Woosley, S.) *Chapter 9 in "Gamma-Ray Bursts* 169–190 (2012).
- [156] Pian, E. *et al.* An optical supernova associated with the X-ray flash XRF 060218. *Nature* **442**, 1011–1013 (2006).
- [157] Starling, R. L. C. *et al.* Discovery of the nearby long, soft GRB 100316D with an associated supernova. *Mon. Not. R. Astron. Soc.* **411**, 2792–2803 (2011).
- [158] Piran, T. The physics of gamma-ray bursts. *Reviews of Modern Physics* **76**, 1143–1210 (2004).
- [159] Khokhlov, A. M. & Ergma, E. V. Peculiar Type-I Supernovae - Explosive Helium Burning in a Low-Mass Accreting White Dwarf. *Soviet Astronomy Letters* **12**, 152–154 (1986).
- [160] Waldman, R. *et al.* Helium Shell Detonations on Low-mass White Dwarfs as a Possible Explanation for SN 2005E. *Astrophys. J.* **738**, 21 (2011).
- [161] Dekany, R. *et al.* The Zwicky Transient Facility: Observing System. *Publ. Astron. Soc. Pac.* **132**, 038001 (2020).
- [162] Bellm, E. C. *et al.* The Zwicky Transient Facility: Surveys and Scheduler. *Publ. Astron. Soc. Pac.* **131**, 068003 (2019).
- [163] Masci, F. J. *et al.* A New Forced Photometry Service for the Zwicky Transient Facility. *arXiv e-prints* arXiv:2305.16279 (2023).
- [164] Lang, D., Hogg, D. W., Mierle, K., Blanton, M. & Roweis, S. Astrometry.net: Blind Astrometric Calibration of Arbitrary Astronomical Images. *Astron. J.* **139**, 1782–1800 (2010).
- [165] Fremling, C. *et al.* PTF12os and iPTF13bvn. Two stripped-envelope supernovae from low-mass progenitors in NGC 5806. *Astron. Astrophys.* **593**, A68 (2016).
- [166] Blagorodnova, N. *et al.* The SED Machine: A Robotic Spectrograph for Fast Transient Classification. *Publ. Astron. Soc. Pac.* **130**, 035003 (2018).
- [167] Rigault, M. *et al.* Fully automated integral field spectrograph pipeline for the SEDMachine: pysedm. *Astron. Astrophys.* **627**, A115 (2019).
- [168] Cenko, S. B. *et al.* The Automated Palomar 60 Inch Telescope. *Publ. Astron. Soc. Pac.* **118**, 1396–1406 (2006).
- [169] Li, W., Filippenko, A. V., Chornock, R. & Jha, S. The Katzman Automatic Imaging Telescope Gamma-Ray Burst Alert System, and Observations of GRB 020813. *Publ. Astron. Soc. Pac.* **115**, 844–853 (2003).
- [170] Filippenko, A. V., Li, W. D., Treffers, R. R. & Modjaz, M. Paczynski, B., Chen, W.-P. & Lemme, C. (eds) *The Lick Observatory Supernova Search with the Katzman Automatic Imaging Telescope*. (eds Paczynski, B., Chen, W.-P. & Lemme, C.) *IAU Colloq. 183: Small Telescope Astronomy on Global Scales*, Vol. 246 of *Astronomical Society of the Pacific Conference Series*, 121 (2001).
- [171] Stahl, B. E. *et al.* Lick Observatory Supernova Search follow-up program: photometry data release of 93 Type Ia supernovae. *Mon. Not. R. Astron. Soc.* **490**, 3882–3907 (2019).
- [172] Stetson, P. B. DAOPHOT - A computer program for crowded-field stellar photometry. *PASP* **99**, 191–222 (1987).
- [173] Steele, I. A. The Liverpool telescope. *Astronomische Nachrichten* **325**, 519–521 (2004).

- [174] Bertin, E. *et al.* Bohlender, D. A., Durand, D. & Handley, T. H. (eds) *The TERAPIX Pipeline*. (eds Bohlender, D. A., Durand, D. & Handley, T. H.) *Astronomical Data Analysis Software and Systems XI*, Vol. 281 of *Astronomical Society of the Pacific Conference Series*, 228 (2002).
- [175] Chambers, K. C. *et al.* The Pan-STARRS1 Surveys. *arXiv e-prints* arXiv:1612.05560 (2016).
- [176] Ahn, C. P. *et al.* The Ninth Data Release of the Sloan Digital Sky Survey: First Spectroscopic Data from the SDSS-III Baryon Oscillation Spectroscopic Survey. *Astrophys. J. Suppl. Ser.* **203**, 21 (2012).
- [177] Roming, P. W. A. *et al.* The Swift Ultra-Violet/Optical Telescope. *Space Sci. Rev.* **120**, 95–142 (2005).
- [178] Gehrels, N. *et al.* The Swift Gamma-Ray Burst Mission. *Astrophys. J.* **611**, 1005–1020 (2004).
- [179] Flewelling, H. A. *et al.* The Pan-STARRS1 Database and Data Products. *Astrophys. J. Suppl. Ser.* **251**, 7 (2020).
- [180] Breeveld, A. A. *et al.* McEnery, J. E., Racusin, J. L. & Gehrels, N. (eds) *An Updated Ultraviolet Calibration for the Swift/UVOT*. (eds McEnery, J. E., Racusin, J. L. & Gehrels, N.) *American Institute of Physics Conference Series*, Vol. 1358 of *American Institute of Physics Conference Series*, 373–376 (2011). [1102.4717](#).
- [181] Stritzinger, M. *et al.* Optical Photometry of the Type Ia Supernova 1999ee and the Type Ib/c Supernova 1999ex in IC 5179. *Astron. J.* **124**, 2100–2117 (2002).
- [182] Oke, J. B. & Gunn, J. E. Secondary standard stars for absolute spectrophotometry. *Astrophys. J.* **266**, 713–717 (1983).
- [183] Schlafly, E. F. & Finkbeiner, D. P. Measuring Reddening with Sloan Digital Sky Survey Stellar Spectra and Recalibrating SFD. *Astrophys. J.* **737**, 103 (2011).
- [184] Cardelli, J. A., Clayton, G. C. & Mathis, J. S. The Relationship between Infrared, Optical, and Ultraviolet Extinction. *Astrophys. J.* **345**, 245 (1989).
- [185] Oke, J. B. *et al.* The Keck Low-Resolution Imaging Spectrometer. *Publ. Astron. Soc. Pac.* **107**, 375 (1995).
- [186] Filippenko, A. V. The importance of atmospheric differential refraction in spectrophotometry. *Publ. Astron. Soc. Pac.* **94**, 715–721 (1982).
- [187] Perley, D. A. Fully Automated Reduction of Longslit Spectroscopy with the Low Resolution Imaging Spectrometer at the Keck Observatory. *Publ. Astron. Soc. Pac.* **131**, 084503 (2019).
- [188] Vernet, J. *et al.* X-shooter, the new wide band intermediate resolution spectrograph at the ESO Very Large Telescope. *Astron. Astrophys.* **536**, A105 (2011).
- [189] Selsing, J. *et al.* The X-shooter GRB afterglow legacy sample (XS-GRB). *Astron. Astrophys.* **623**, A92 (2019).
- [190] van Dokkum, P. G. Cosmic-Ray Rejection by Laplacian Edge Detection. *Publ. Astron. Soc. Pac.* **113**, 1420–1427 (2001).
- [191] Goldoni, P. *et al.* McLean, I. S. & Iye, M. (eds) *Data reduction software of the X-shooter spectrograph*. (eds McLean, I. S. & Iye, M.) *Society of Photo-Optical Instrumentation Engineers (SPIE) Conference Series*, Vol. 6269 of *Society of Photo-Optical Instrumentation Engineers (SPIE) Conference Series*, 62692K (2006).

- [192] Modigliani, A. *et al.* Silva, D. R., Peck, A. B. & Soifer, B. T. (eds) *The X-shooter pipeline*. (eds Silva, D. R., Peck, A. B. & Soifer, B. T.) *Observatory Operations: Strategies, Processes, and Systems III*, Vol. 7737 of *Society of Photo-Optical Instrumentation Engineers (SPIE) Conference Series*, 773728 (2010).
- [193] Oke, J. B. & Gunn, J. E. An Efficient Low Resolution and Moderate Resolution Spectrograph for the Hale Telescope. *Publ. Astron. Soc. Pac.* **94**, 586 (1982).
- [194] Prochaska, J. *et al.* PypeIt: The Python Spectroscopic Data Reduction Pipeline. *The Journal of Open Source Software* **5**, 2308 (2020).
- [195] Prochaska, J. X. *et al.* pypeit/PypeIt: Release 1.0.0 (2020).
- [196] Silverman, J. M. *et al.* Berkeley Supernova Ia Program - I. Observations, data reduction and spectroscopic sample of 582 low-redshift Type Ia supernovae. *Mon. Not. R. Astron. Soc.* **425**, 1789–1818 (2012).
- [197] Burrows, D. N. *et al.* The Swift X-Ray Telescope. *Space Sci. Rev.* **120**, 165–195 (2005).
- [198] Evans, P. A. *et al.* An online repository of Swift/XRT light curves of  $\gamma$ -ray bursts. *Astron. Astrophys.* **469**, 379–385 (2007).
- [199] Evans, P. A. *et al.* Methods and results of an automatic analysis of a complete sample of Swift-XRT observations of GRBs. *Mon. Not. R. Astron. Soc.* **397**, 1177–1201 (2009).
- [200] HI4PI Collaboration *et al.* HI4PI: A full-sky H I survey based on EBHIS and GASS. *Astron. Astrophys.* **594**, A116 (2016).
- [201] Martin, D. C. *et al.* The Galaxy Evolution Explorer: A Space Ultraviolet Survey Mission. *Astrophys. J.* **619**, L1 (2005).
- [202] Wright, A. H. *et al.* Galaxy And Mass Assembly: accurate panchromatic photometry from optical priors using LAMBDA. *Mon. Not. R. Astron. Soc.* **460**, 765 (2016).
- [203] McMahan, R. G. *et al.* First Scientific Results from the VISTA Hemisphere Survey (VHS). *The Messenger* **154**, 35–37 (2013).
- [204] Skrutskie, M. F. *et al.* The Two Micron All Sky Survey (2MASS). *Astron. J.* **131**, 1163–1183 (2006).
- [205] Pastorello, A. *et al.* Massive stars exploding in a He-rich circumstellar medium - IV. Transitional Type Ibn supernovae. *Mon. Not. R. Astron. Soc.* **449**, 1921–1940 (2015).
- [206] Nicholl, M. SuperBol: A User-friendly Python Routine for Bolometric Light Curves. *Research Notes of the American Astronomical Society* **2**, 230 (2018).
- [207] Gagliano, A. *et al.* An Early-time Optical and Ultraviolet Excess in the Type-Ic SN 2020oi. *Astrophys. J.* **924**, 55 (2022).
- [208] Swartz, D. A., Sutherland, P. G. & Harkness, R. P. Gamma-Ray Transfer and Energy Deposition in Supernovae. *Astrophys. J.* **446**, 766 (1995).
- [209] Wang, S. Q., Wang, L. J., Dai, Z. G. & Wu, X. F. Superluminous Supernovae Powered by Magnetars: Late-time Light Curves and Hard Emission Leakage. *Astrophys. J.* **799**, 107 (2015).